SET-UP AND CALIBRATION OF A KINEMATIC COINCIDENCE SYSTEM FOR LOW-ENERGY LIGHT HEAVY-ION REACTIONS: MEASUREMENT OF $^{10}B\ (^{6}Li, \alpha)\ ^{12}C$

Mistura Bolaji Ajani

A Research Report submitted to the Faculty of Science,
University of the Witwatersrand, Johannesburg,
in partial fulfilment of the requirements for the degree of
Master of Science

Johannesburg, 2017

I declare that this research report is my own, unaided work. It is being submitted in partial fulfilment of the requirements for the degree of Master of Science in the University of the Witwatersrand, Johannesburg. It has not been submitted before for any degree or examination in any other University.

Signature: ______________________

Mistura Bolaji Ajani

Date: February 02, 2017

Abstract

Light heavy-ion scattering reactions at tandem energies require unambiguous particle identification of reaction products. As such, a kinematic coincidence system was set-up between a silicon surface-barrier position sensitive detector and heavy-ion silicon surface-barrier detector. The system was calibrated using ^{12}C + ^{12}C elastic scattering at the incident projectile laboratory energy E_{Lab} (^{12}C) = 22.5 MeV using a ^{12}C beam provided by the EN tandem Van de Graaff accelerator of iThemba LABS (Gauteng). This was a necessary step prior to investigating for the first time the possibility of a measurable cross-section for the ^{10}B (^{6}Li, α_n) ^{12}C reaction at the limited maximum beam energy available of up to E_{Lab} (^{6}Li) = 20 MeV. The deuteron transfer reaction has, however, a large positive Q-value of 23.7 MeV which produces α-particles at energies up to about 40 MeV. Spin selectivity of the reaction produced a measurable yield to the first excited state in ^{12}C (2_1^+, 4.43 MeV) with the ground state ^{12}C (0_1^+, g.s.) being about an order of magnitude lower. As expected, states above the ^{12}C (2_1^+, 4.43 MeV) state were not seen as they are above the 3α break-up threshold of 7.65 MeV. It is thus conjectured that by measuring the α-particles directly, the 2^+ excitation of the Hoyle state ^{12}C (0_2^+, 7.65 MeV) may be observed in future experiments.

Dedication

Dedicated to my lovely parents Mr. and Mrs. Owoyemi Ajani for their moral and financial support over the years.

Acknowledgements

Firstly I would like to express my profound gratitude to Almighty Allah, the one who knows every end from its very beginning, the one who has preserved my life and made it possible for me to successfully complete this study. *Ya-Allah* to you I say *Alhamdullillah*.

My immense thanks go to my principal supervisor Prof. John Cater and co-supervisor Dr. Iyabo Usman whose constant guidance, all-encompassing support and encouragement have culminated to make this study a resounding success. Thank you for your fatherly and motherly care, without your cooperation the success of this journey would not have been achievable. Thank you for always being there for me, I am most obliged.

To Mr. Gerhard Badenhorst, Mr. Fritz Balzun, Mr. Oleg Pekar, Mrs. Duduzile and Mrs. Mahlare, of iThemba LABS, thank you for your support at the experimental level of this study. I am very grateful.

To my parents, Mr. and Mrs. Owoyemi Ajani and my lovely siblings, thank you for your financial support and emotional support from the beginning of this journey till its very end. Thank you for believing in me, I am most obliged.

To my Mentors, Dr. Mahboob Adekilekun and Dr. Kehinde Adekilekun, thank you for your guidance, admonition and support from the point of making a career choice up till this present stage in my academic life. I am very grateful.

To my best friend and companion, Mr. Omoyemi Babarinde, thank you for believing in the success of this journey, I appreciate your encouragement and unwavering support. Indeed love is a treasure that can only be bought by giving it away.

To Modupe Adebawo and Pheladi Topsy Molema, thank you for your dependable, valuable friendship and for being there throughout the course of this journey, thank you for your emotional support and encouragement. Indeed burdens are lighter when shared.

To Mr. M.B. Latif, My brother from another mother, thank you for your immeasurable contribution towards the success of this research. *Olorun asan yin lesan rere.*

To Dr. Jingo, Dr. Kureba and Dr. Donaldson. Thank you for your contribution towards the success of this journey, may God bless you all.

Also I am grateful to the family of Prof. Pedro for their love, encouragement and financial supports.

Lastly, I would like to thank my colleagues in school of physics for such wonderful memories we shared and fun time we had together.

Table of Contents

Contents **Page**

List of Figures

List of Tables

CHAPTER 1

Introduction

Light heavy-ion reactions on low mass targets at incident energies close to and just above the Coulomb barrier yield many reaction products. This has provided over many decades now a powerful tool for investigating nuclear structure properties. In particular, tandem accelerator laboratories have played an important role world-wide in this area of basic nuclear structure physics. Typically, beams ranging from protons and α-particles up to calcium ions and targets ranging in mass up to about iron have been employed. The EN tandem Van de Graaff laboratory of iThemba LABS (Gauteng) (formally the Schonland Institute, University of the Witwatersrand) provides such a resource for the present project. The kinematic coincidence technique is particularly powerful for identifying reaction products formed in light heavy-ion scattering experiments. As a first step in the present project, a silicon surface-barrier position sensitive detector was used together with a heavy-ion silicon surface-barrier detector to set-up a kinematic coincidence system. This system was first checked and calibrated using $^{12}C + ^{12}C$ elastic scattering.

However, the main part of the project was to investigate the deuteron transfer reaction of ^{10}B (^{6}Li, α_n) ^{12}C with a view to identifying, if possible, the population of the ground state of ^{12}C, the first 0^+ state, ^{12}C (0_1^+, g.s.) and the first 2^+ excited state as the first excited state of ^{12}C as ^{12}C (2_1^+, 4.43 MeV). States excited in ^{12}C above the first 2^+ excited state would not survive to be measured in coincidence with the corresponding α-particle since the excited state of ^{12}C would be above the 3α break-up threshold.

Interest in the present reaction measurement stems from the recent experimental work to identify excited states of the Hoyle state [FRE09]. In 1954 Sir Fred Hoyle predicted the existence of a 0^+ excited state in ^{12}C as a requirement for the build-up of carbon in the core of stars. This state was soon thereafter discovered and is known as the Hoyle state ^{12}C (0_2^+, 7.65 MeV). Subsequently, stellar models required the existence of excited states of the Hoyle state to account for the rapid build-up of carbon in stars. The 2^+ excited state of the Hoyle state was recently identified to lie at E_x = 9.75 MeV [FRE09] directly underneath the dominant 3_1^- in ^{12}C at the E_x = 9.64 MeV.

The present experimental work seeks to determine if the transfer reaction ^{10}B (^{6}Li, α_n) ^{12}C does populate the 0_1^+ and 2_1^+ states in ^{12}C strongly enough at the energies available at the tandem as a prelude to further experimentation using the other techniques for measurement of excited states of the Hoyle state.

The research report is organised as follows:

- Chapter 2 describes the theoretical aspect of nuclear elastic scattering, kinematics of nuclear reactions, the Hoyle state of ^{12}C and excited states of the Hoyle state, transfer reactions and excitation of ^{12}C using the ^{10}B (^{6}Li, α_n) ^{12}C* reaction.

- Chapter 3 presents the experimental lay-out of the EN tandem Van de Graaff accelerator, the beam line and large scattering chamber, the coincidence system set-up for ^{12}C + ^{12}C elastic scattering and the ^{10}B (^{6}Li, α_n)^{12}C* reaction, data acquisition system and data extraction.

- Chapter 4 describes the experimental results, analysis and discussion.

- A summary of the conclusions are detailed in Chapter 5.

CHAPTER 2

Theoretical aspects

This chapter is related to theoretical aspects of nuclear elastic scattering, inelastic scattering and transfer reactions. In particular, an appreciation of the Hoyle-state of ^{12}C and its role in the production of ^{12}C in the core of stars is required.

2.1 Nuclear elastic and inelastic scattering

At incident energies below the Coulomb barrier nuclear elastic scattering is dominated by Coulomb scattering or Rutherford scattering. While at energies close to and above the Coulomb barrier nuclear effects become important resulting in the Optical Model phenomenological description of elastic scattering. Inelastic scattering may leave either the projectile or the target nucleus, or both in an excited state. A basic description of these processes is described below.

2.1.1 Rutherford scattering

Rutherford scattering is the elastic scattering of charged particles by the Coulomb interaction [JEL90]. Figure 2.1 shows a Coulomb trajectory for Rutherford scattering, where b is the impact parameter from the nucleus in the absence of a repulsive force and is scattered through an angle θ. The differential scattering cross-section can be derived from the equation of motion for a particle interacting with a central potential. The following equation shows the differential cross-section for Rutherford scattering [WIL91]:

$$\frac{d\sigma}{d\Omega_{\text{c.m.}}} = \left(\frac{Z_1 Z_2 e^2}{4\pi\varepsilon_o}\right)\left(\frac{1}{4E_{\text{c.m.}}}\right)^2 \left(\frac{1}{\sin^4 \frac{\theta_{\text{c.m}}}{2}}\right), \tag{2.1}$$

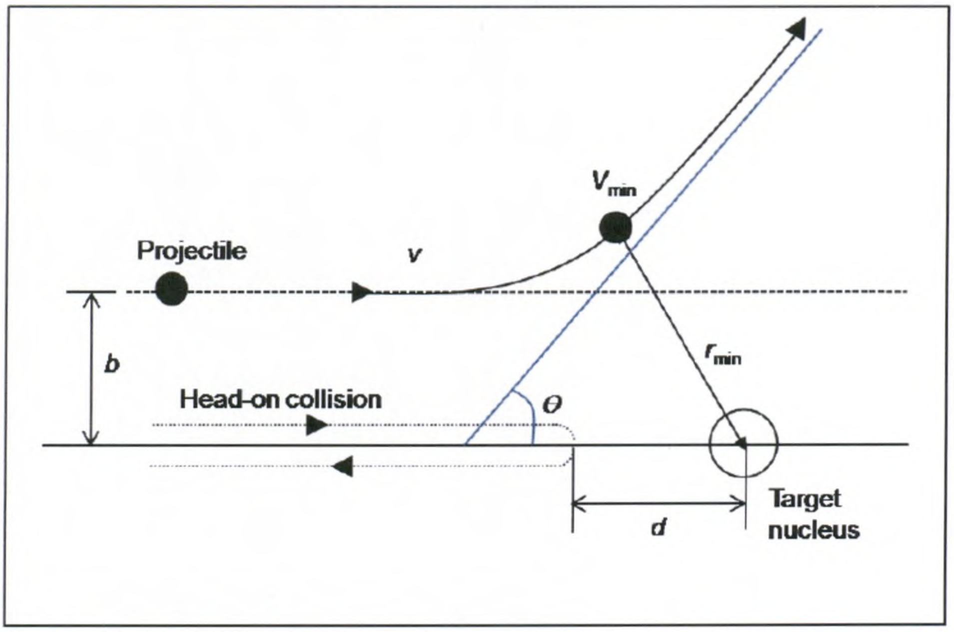

Figure 2.1: Coulomb trajectory for Rutherford scattering [JIN10].

where $Z_1 e$ is the charge of the projectile, $Z_2 e$ is the charge of the target, $\theta_{c.m.}$ is the centre-of-mass scattering angle and $E_{c.m.}$ is the centre-of-mass energy of the projectile. The above equation shows that Rutherford scattering cross section depends on the scattering angle and is independent of the spin of the projectile and the target.

The relationship between the impact parameter and scattering angle is given by [KRA88]:

$$b = \frac{d}{2} \cot \frac{\theta}{2}, \tag{2.2}$$

where d is the distance of the closest approach.

2.1.2 Optical Model of the elastic scattering

The Optical Model of the elastic scattering describes the interaction of nuclei in the presence of the strong nuclear force [SAT80]. The interaction of the nucleons is replaced by a two-body interaction U(r) between the incident projectile and the target nucleus, which is given as [HOD78]:

$$U(r) = U_{\mathrm{C}}(r) + U_{\mathrm{N}}(r)\,, \tag{2.3}$$

where $U_{\mathrm{C}}(r)$ is the Coulomb potential due to a uniformly charge sphere. Here, the nuclear scattering potential is generally expressed as

$$U_{\mathrm{N}}(r) = [V(r) + iW(r)]\,, \tag{2.4}$$

where the imaginary part takes into account absorption into non-elastic scattering channels. Typically, a Wood-Saxon form is used for both the real and the imaginary parts and is given by:

$$U = V_0 f_{\mathrm{R}}(r) + iW_0 f_{\mathrm{I}}(r)\,, \tag{2.5}$$

$$f_{\mathrm{R,I}}(r) = \left[1 + \exp\left(\frac{r - R_{\mathrm{R,I}}}{a_{\mathrm{R,I}}}\right)\right]^{-1}, \tag{2.6}$$

where V_0 and W_0 are the potential depths of the real and imaginary parts, $R_{\mathrm{R,I}}$ are the radius parameters of the real and the imaginary parts and $a_{\mathrm{R,I}}$ are the real and imaginary diffusenesses, respectively. Volume absorption results from the use of Eq. (2.6). An imaginary potential with surface absorption is given by [KRA88]:

$$W(r) = -W_1 \frac{d}{dr}\left[1 + \exp\left(\frac{r - R_{\mathrm{I}}}{a_{\mathrm{I}}}\right)\right]^{-1}. \tag{2.7}$$

Here, the imaginary potential has a surface peak since the valence nucleons at the surface can easily participate in nuclear reactions. Due to the Pauli Exclusion Principle, the tightly bound nucleons in the interior would not participate [AUE78]. The radii in Eq. (2.6) are expressed in terms of the mass number A_1 and A_2 of the projectile and the target nuclei, respectively, and the corresponding radius parameters $r_{0\mathrm{R,I}}$ and are given by:

$$R_{R,I} = r_{0R,I}\left[A_1^{1/3} + A_2^{1/3}\right]. \tag{2.8}$$

Solution of the Schrödinger equation using the optical model potential yields the elastic scattering cross-section is discussed in [JAC70].

2.2 Kinematics of nuclear reactions

For a nuclear reaction to occur, an incident particle or a projectile interacts with the target nucleus as illustrated in Fig. 2.2. It is necessary to introduce the ground state Q-value of the reaction which is determined as the difference between the initial and final masses [KRA88]:

$$Q = (M_1 + M_2 - M_3 - M_4)c^2. \tag{2.9}$$

By using available computer programmes e.g. CATKIN [CAT05] the equations of Fig. 2.2 can easily be evaluated.

Kinematics of nuclear reactions and scattering

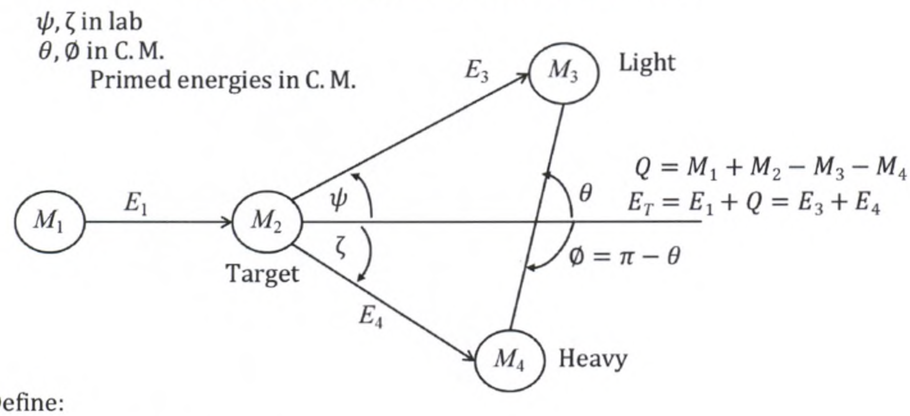

Define:

$$A = \frac{M_1 M_4 (E_1/E_T)}{(M_1+M_2)(M_3+M_4)}, \quad C = \frac{M_2 M_3}{(M_1+M_2)(M_3+M_4)}\left(1 + \frac{M_1 Q}{M_2 E_T}\right) = \frac{E_4'}{E_T}$$

$$B = \frac{M_1 M_3 (E_1/E_T)}{(M_1+M_2)(M_3+M_4)}, \quad D = \frac{M_2 M_4}{(M_1+M_2)(M_3+M_4)}\left(1 + \frac{M_1 Q}{M_2 E_T}\right) = \frac{E_3'}{E_T}$$

Note that $A + B + C + D = 1$ and $AC = BD$

Lab energy of light product:	$\frac{E_3}{E_T} = B + D + 2(AC)^{1/2}\cos\theta$ $= B\left[\cos\psi \pm (D/B - \sin^2\psi)^{1/2}\right]^2$	Use only plus sign unless $B > D$, in which case $\psi_{max} = \sin^{-1}(D/B)^{1/2}$
Lab energy of heavy product:	$\frac{E_4}{E_T} = A + C + 2(AC)^{1/2}\cos\phi$ $= A\left[\cos\zeta \pm (C/A - \sin^2\zeta)^{1/2}\right]^2$	Use only plus sign unless $A > C$, in which case $\zeta_{max} = \sin^{-1}(C/A)^{1/2}$
Lab angle of heavy product:	$\sin\zeta = \left(\frac{M_3 E_3}{M_4 E_4}\right)^{1/2}\sin\psi$	$\sin\theta = \left(\frac{E_3 E_T}{D}\right)^{1/2}\sin\psi$

Figure 2.2: A diagram taken from Marion and Young [MAR68] illustrating nuclear reaction kinematics and associated formulae.

2.3 The Hoyle state of ^{12}C and excited states of the Hoyle state

The second 0^+ state of ^{12}C was predicted by Hoyle in 1954 [HOY54], playing a vital role in the production of ^{12}C in stars. The majority of the heavy elements in the universe are believed to originate in the nucleosynthesis which occurs during supernovae and other explosive astrophysical phenomena. The carbon abundance is due to 3α-process in stars. The 3α-process is a nuclear fusion reaction which transforms 3α-nuclei into ^{12}C. From the diagram shown in Fig. 2.3, the stage one reaction of 3α-process is 2α-particles fusing to form ^{8}Be. Further, ^{8}Be is unstable and has a Q-value of -97.3 keV and later decays into 2α-particles with a lifetime of $\sim 10^{-16}$ s. Red giant stars provide hydrostatic burning of helium into carbon which is governed completely by a single resonance in ^{12}C, the Hoyle state. The ground state of ^{8}Be lies 92 keV above the α decay threshold with a width of 5.6 eV implying a lifetime of about 10^{-16} s. The energy of 92 keV which lies close to the Gamow window of α burning temperatures is nearly equal to 10^{8} K [KAR16]. The Gamow window shown in Fig. 2.4 is a convolution of the Maxwell-Boltzmann velocity distribution and quantum mechanical tunneling through the Coulomb barrier. In a given stellar environment, the α-particle nuclear reactions are taking place in the energy window around the E_o effective energy

$$E_o = \left(\frac{bkT}{2}\right)^{2/3}, \tag{2.10}$$

where b is the corresponding barrier penetrability, k is the fundamental Boltzmann constant and T is the plasma temperature.

This is the well-known Gamow peak, shifting towards higher energies with increasing stellar temperature. Further, the energy of the Hoyle state lies at 285 keV above the $^{8}Be + \alpha$ decay threshold. This corresponds to the Gamow window peak for temperatures close to 2.5 x 10^{8} K. Also, the region for synthesis of ^{12}C is crucial provided the enhancement is approximately eight orders of magnitude. [FRE14] . Typically, the considerations here are limited for low-energy direct captures and high-energy compound nucleus reactions.

The important contributions in these regions are still natural parity states and the corresponding direct reactions. For the high temperature the importance of the individual contributions is determined by the available states in ^{12}C and ^{8}Be within the Gamow window. The different possible contributions are 0^{+} and 2^{+}

strength in ^{8}Be and 0^+, 1^-, 2^+ and 3^- in ^{12}C strength. These contributions are all listed and discussed by Buchmann and Barnes [BUC06]. The 2^+ state in this energy region is seen as the first rotational excitation. Such a state, however, remains undetected experimentally. This is supposed to be the 2^+ excited state of 0^+ state at 7.6 MeV [MAR08]. In addition, the 2^+ state at 9.2 MeV, which at temperatures nearly equal to 10^8 K significantly speed up the 3α process in red giant stars [FYN04].

An excitation energy level diagram for ^{12}C is shown in Fig. 2.5. The nature of 3α-cluster configurations in ^{12}C has been discussed in [FRE12] and the possibility of collective excitations leading to a 2^+ excitation of the Hoyle state. Experimental evidence for the 2^+ excitation state of Hoyle state has been discussed in [FRE09, FRE12, ZIM13, FRE14] and reference therein.

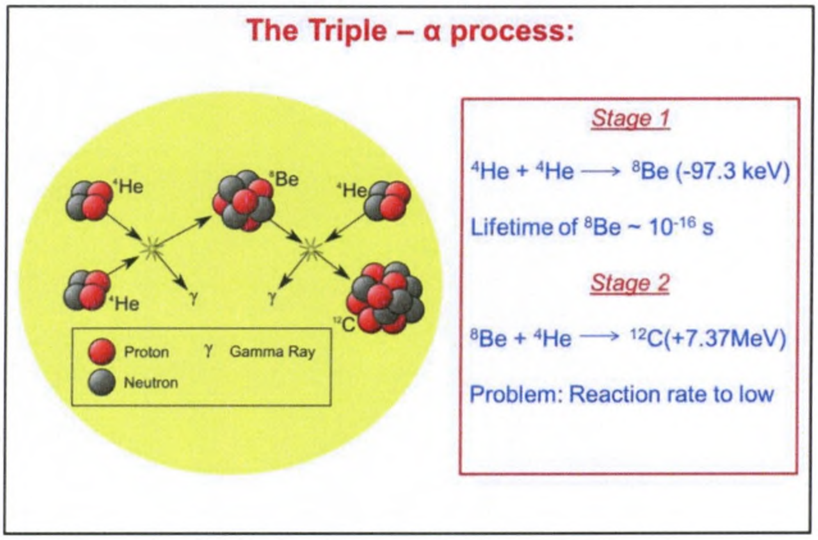

Figure 2.3: The triple- α process for post main sequence stars [OST07].

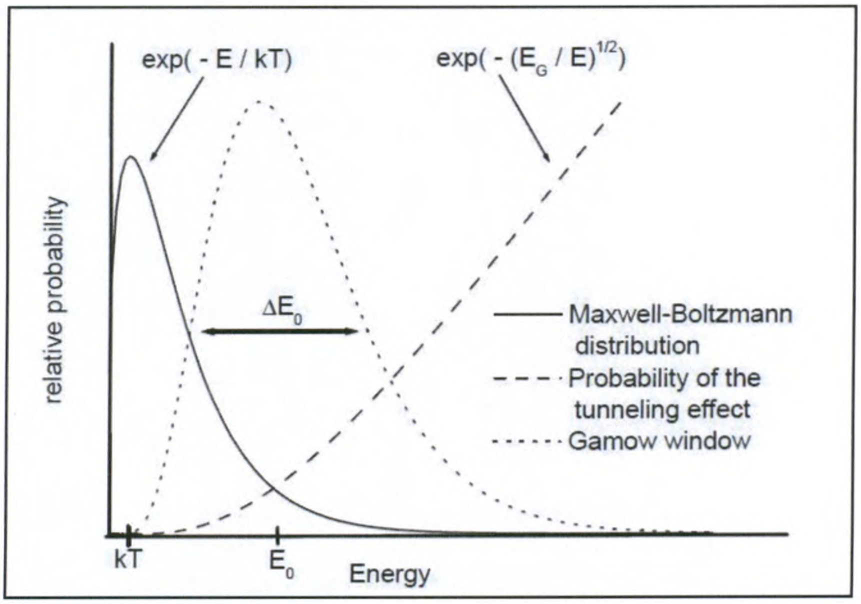

Figure 2.4: The Maxwell-Boltzmann distribution and the probability of the tunneling effect produces what is known as Gamow window, where the nuclear reaction occur in stars [GAB08].

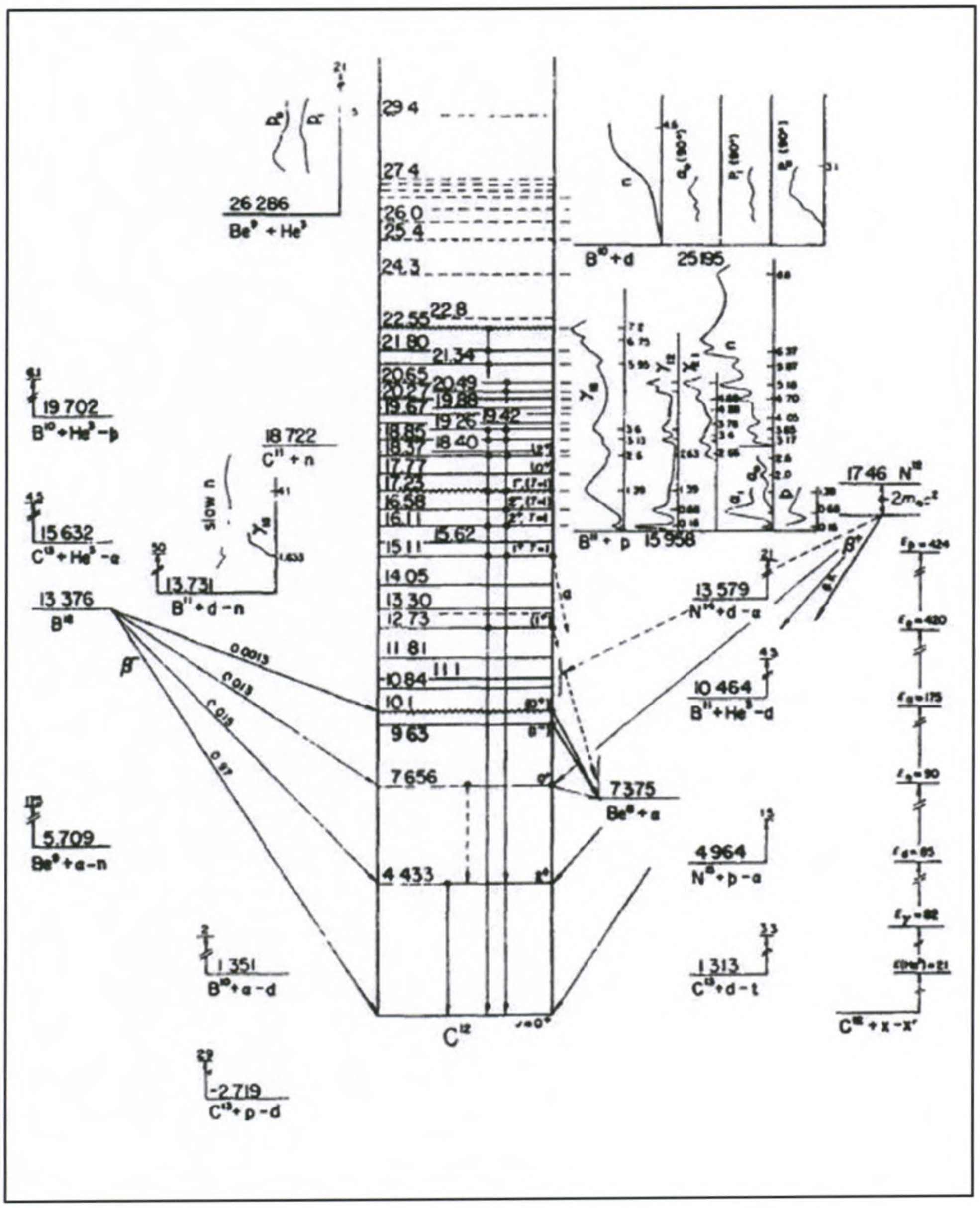

Figure 2.5: Energy level diagram of ^{12}C [AJZ59].

2.4 Transfer reactions and excitation of ^{12}C using the $^{10}B\,(^{6}Li, \alpha_n)\,^{12}C^*$ reaction

Direct reactions can be classified into two main categories namely:

- inelastic excitation of projectile and/or target and
- transfer reactions.

The general way of writing nuclear reactions is given as

$$A(a, b)B\ , \tag{2.13a}$$

where A is the target, a is the projectile, b is the projectile related product and B is the target related product.

Transfer reactions can be described as a special case of direct reactions where one or more nucleons are transferred from the projectile or the target nucleus to form new final products, generally different from the initial products. In this particular experiment, the nuclear reaction is as follows:

$$\begin{array}{c} 3^+ \quad 1^+ \quad 0^+ \quad 0^+, 2^+, 3^- \ldots \\ ^{10}B\,(\underbrace{^{6}Li}_{\alpha\,+\,d},\ \alpha)\ \underbrace{^{12}C}_{^{10}B\,+\,d} \\ 0^+ \quad 1^+ \quad 3^+ \quad 1^+ \end{array} \ . \tag{2.13b}$$

This is a stripping reaction where the ^{6}Li is seen as a tightly bound α-core orbited by a deuteron. Further, the heavy product (^{12}C) is seen as ^{10}B and a deuteron.

The theory of Distorted Wave Born Approximation (DWBA) gives a good description for nuclear transfer reaction. As indicated in Eq. (2.13a), the projectile a is treated as a composite system $a = b + x$, where x may be a nucleon or a few nucleon cluster. The cluster x transferred from the projectile to the target leads to formation of the composite target-like fragment in the exit channel $B = A + x$ (see Fig. 2.6). Here, all particles may be non zero spin given as J_A, J_B, j_a, j_b and j_x.

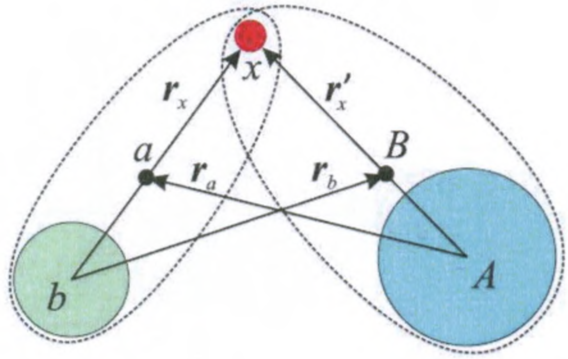

Figure 2.6: The coordinate system transfer for a scattering reaction [ZAG16].

The differential cross-section is obtained from the transition amplitude as [ZAG16]:

$$\frac{d\sigma}{d\Omega}(\theta)=\left[\frac{\mu_\alpha\mu_\beta}{\left(2\pi\hbar^2\right)^2}\right]^2\frac{k_\beta}{k_\alpha}\frac{1}{(2J_A+1)(2j_a-1)}\sum_{M_AM_Bm_am_b}\left|T_{M_AM_Bm_am_b}\right|^2, \tag{2.14}$$

where k_β and k_α is the initial and final momentum of the bombarding particle after the scattering, μ is the reduced mass, T_{fi} is the transition amplitude that described the transfer from an initial state (i) of the two fragments to a final internal state (f) given by [ZAG16]:

$$T_{fi}^{\alpha(\beta)}=\mathrm{J}\iint d^3r_b d^3r_a \mathrm{X}_{k_f}^{(-)*}(r_b)\langle bB|\Delta V_{\alpha(\beta)}|aA\rangle \mathrm{X}_{k_i}^{(+)}(r_a). \tag{2.15}$$

where $\mathrm{X}_{k_i}^{(+)}$ and $\mathrm{X}_{k_f}^{(-)}$ are the initial and final distorted waves, respectively, which can be generated before and after collision, r_a and r_b are the coordinates for (*a, A*) and (*b, B*) as indicated in Fig. 2.6 and ϑ is the Jacobian for the coordinates of transformation.

The quantity $\langle bB|\Delta V_{\alpha(\beta)}|aA\rangle$ shown in Eq. (2.15) is the form factor for transfer reactions that couple the bound states in the entrance and exit channels and is calculated in the post (β) or prior(α) form. The calculation for the transfer cross-sections is beyond the scope of the present project.

CHAPTER 3

Experimental considerations

The experimental details are presented for elastic scattering of $^{12}C + ^{12}C$ and the deuteron transfer reaction of $^{6}Li + ^{10}B$ using carbon and lithium beams delivered from EN tandem Van de Graaff accelerator of iThemba LABS (Gauteng). In this chapter the experimental equipment and techniques used in carrying out the experiments will be discussed.

3.1 EN tandem Van de Graaff accelerator lay-out

The main facility for all the experiments performed at iThemba LABS (Gauteng) is the 6 MV tandem accelerator. A diagrammatic lay-out of the accelerator facility is shown in Fig. 3.1. The beams used for the experiments were from a caesium sputtering negative-ion source directed into the inflection magnet for injection into the tandem accelerator. The centre terminal of the tandem accelerator can be charged to a voltage of up to +6 MV by the two pelletron chains. The negative-ion beam passes through a gas stripper canal at the centre terminal and the required charge state, which is selected by the analysing magnet, is then transported to the scattering chamber via the switching magnet.

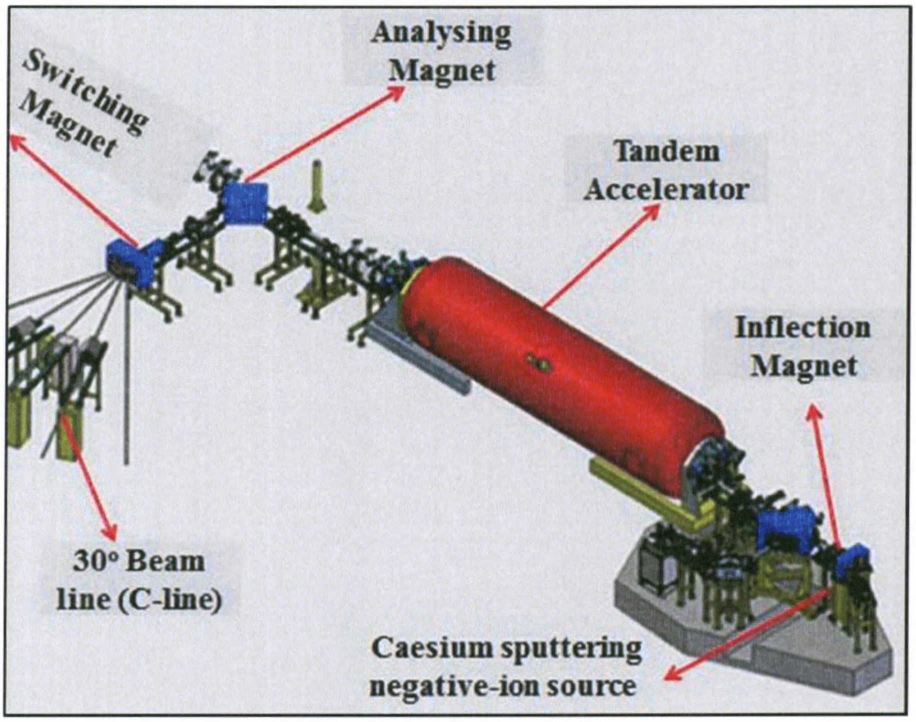

Figure 3.1: Schematic lay-out of EN tandem Van de Graaff accelerator of iThemba LABS (Gauteng).

3.1.1 Production of ^{12}C beams

A model 860A caesium sputter ion source from the General Ionex Corporation was used to produce a beam of $^{12}C^-$. Carbon forms a very prolific negative ion beam from a sintered carbon right-cylinder pushed into a cylindrical copper holder. A source output of about 6 to 12 μA of $^{12}C^-$ was injected into the accelerator *via* the inflection magnet and the 4^+ charge state was selected by the analyser magnet after acceleration to produce a ^{12}C beam at E_{Lab} = 22.5 MeV from a 4.5 MV terminal, to be directed into the large scattering chamber.

3.1.2 Production of ^{6}Li beams

The $^6Li^-$ ions were produced by the 860 A ion source by using $^6LiO_2$ as cathode material. The $^6Li^-$ current was usually less than 2 μA and the beam current on the target was about 10 enA of $^6Li^{3+}$.

3.2 Experimental beam line and large scattering chamber

A diagrammatic lay-out of the experimental beam line used is shown in Fig. 3.2. Corresponding photographs of the large scattering chamber with components identified are shown in Figs. 3.3 and 3.4. The ^{12}C or ^{6}Li beams are transported from the tandem accelerator to the C-line and can be observed using Faraday cups for alignment and transmission into the scattering chamber. The beam is focused down the C-line by a quadrupole magnet. Also, the beam was defined by a circular collimator with a diameter of 1 mm at the entrance port of the scattering chamber after a square aperture of side length 20 mm shown in Fig. 3.2. The square aperture was created by a system of slits upstream of the entrance collimator. The entrance collimator with the line slits (adjusted manually) determines the beam divergence at the target.

The large scattering chamber contains a target ladder, position sensitive detector and heavy ion detector. The target ladder contains a ^{241}Am α-source, two ^{12}C and two ^{10}B targets. The beam scattered from the target was detected by a Position Sensitive Detector (PSD) and Heavy-Ion (HI) detector which are attached to the turntable parts of the large scattering chamber.

3.2.1 Production of ^{12}C targets

The ^{12}C targets used in this experiment were of areal density of 32 $\mu g/cm^2$ and 50 $\mu g/cm^2$ and were self-supporting. The carbon was produced from a carbon arc which is deposited onto a microscope slide in vacuum. The release agent was water soluble and had been deposited previously onto the slide.

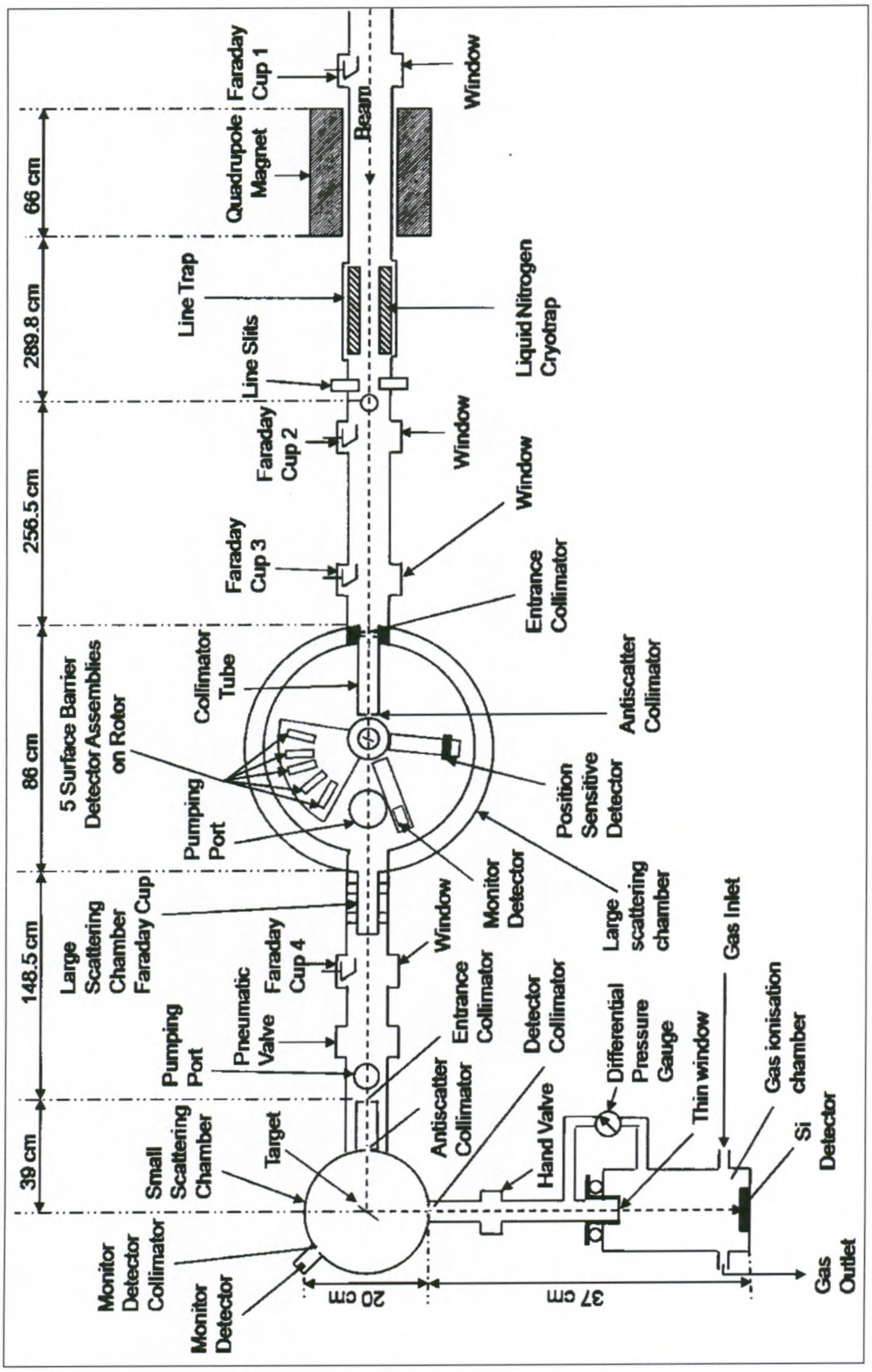

Figure 3.2: Experimental setup with the C-line equipment at the EN tandem Accelerator of the iThemba LABS (Gauteng) [JIN10].

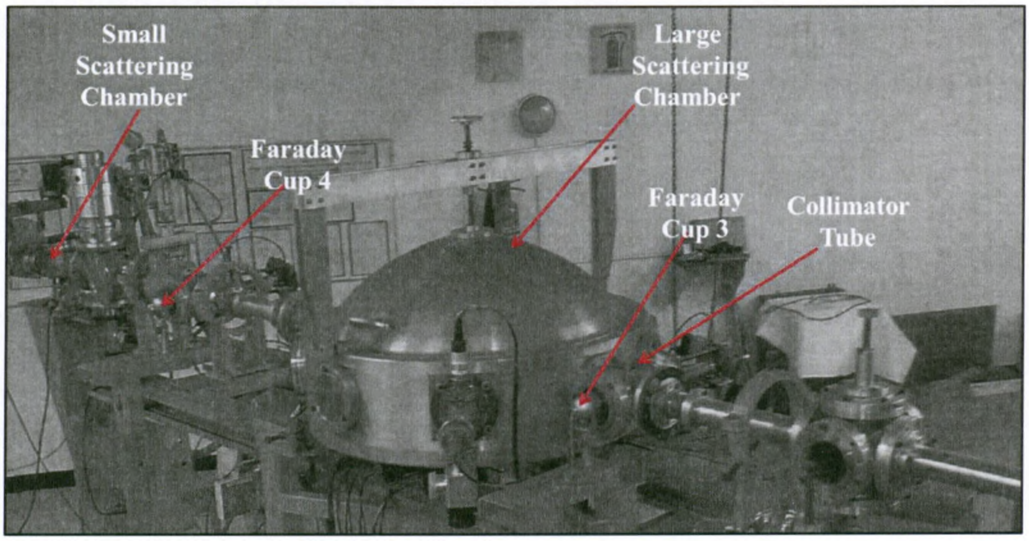

Figure 3.3: Beam line set-up and the large scattering chamber.

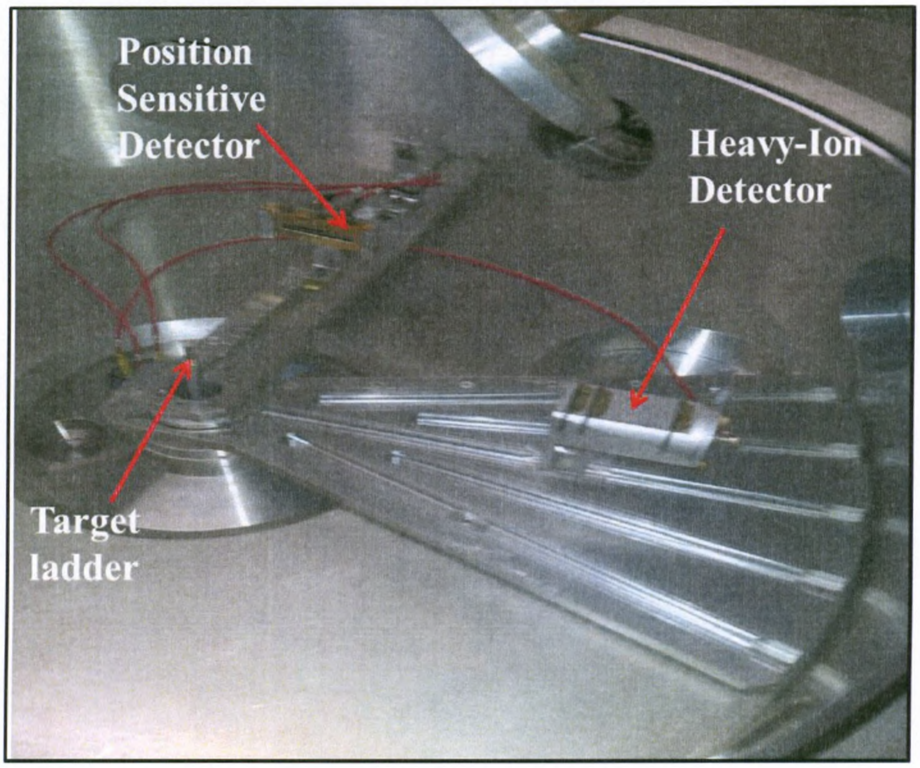

Figure 3.4: Photograph of the inner part of the scattering chamber showing target ladder, PSD and HI detector.

3.2.2 Production of ^{10}B targets

Boron targets were manufactured using the vacuum evaporation method. This was achieved by heating the crystalline pellets of ^{10}B by an electron gun. A polished stainless steel plate was used as substrate. It should be noted that the material has a low vapour pressure and high melting point, therefore, the pressure was maintained below 1×10^{-5} mmHg. Deposited films were floated off from the substrate and the self-supporting ^{10}B targets were about 50 μg/cm^2 areal density [KHE15].

3.3 Coincidence system HI-PSD set-up for ^{12}C + ^{12}C elastic scattering and the ^{10}B (^{6}Li, α_n)^{12}C* reaction

The kinematic coincidence method for elastic scattering and transfer reaction studies leads to an unambiguous identification of reaction products.

3.3.1 Kinematic coincidence system for ^{12}C + ^{12}C elastic scattering

Figure 3.5 shows the typical diagram for ^{12}C + ^{12}C where $\theta_{\rm HI} + \theta_{\rm PSD} = 90°$ for elastic scattering. A Position Sensitive Detector (PSD) mounted on a single movable arm was set-up in coincidence with a Heavy-Ion detector (HI) at $\theta_{\rm Lab}$ = 50°. The distance from the target to the HI surface barrier detector was 250 mm and the beam geometry set-up from the target was calculated to be $\Delta\theta_{\rm PSD} = 15.2°$.

3.3.2 Kinematic coincidence system for ^{10}B (^{6}Li, α_n)^{12}C reaction

The ^{6}Li + ^{10}B can yield α + ^{12}C as shown in Fig. 3.6. The α_0, α_1, α_2, α_3 and α_4 kinematic values obtained from the geometry of the set-up are given in Table 3.1, corresponding to $\theta_{\rm c.m.} \approx 90^{\rm o}$. The angular range for α_0 - α_4 is 13.7$^{\rm o}$ and is within the angular acceptance of the PSD. The various kinematic values for the reaction studies were calculated using the kinematic programme CATKIN [CAT05] (see Section 2.2).

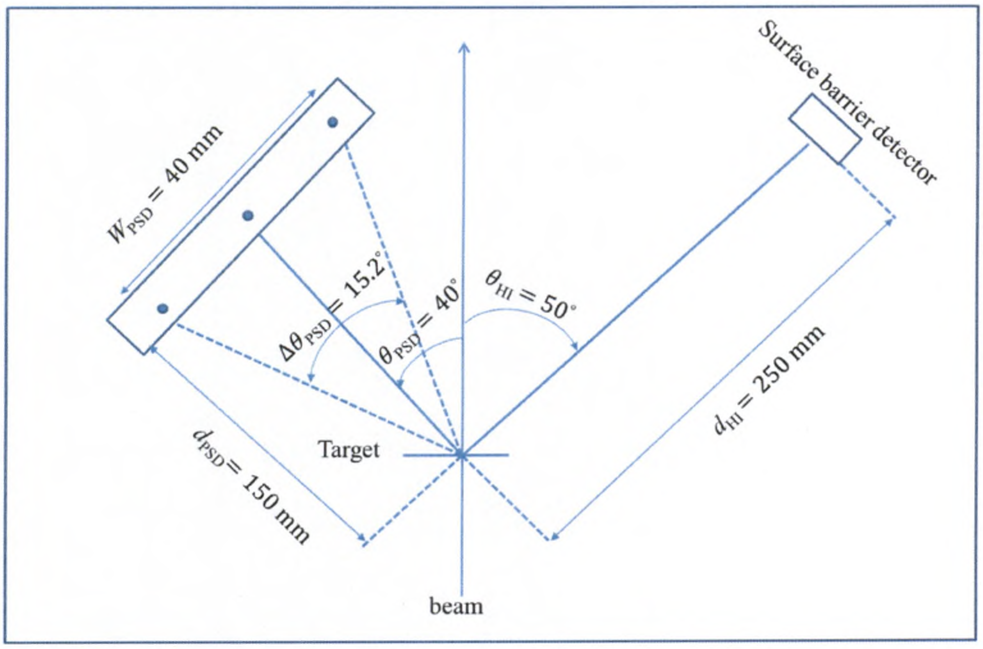

Figure 3.5: A typical kinematic coincidence set-up for ^{12}C + ^{12}C at $\theta_{HI} + \theta_{PSD} =$ 90° for elastic scattering coincidence.

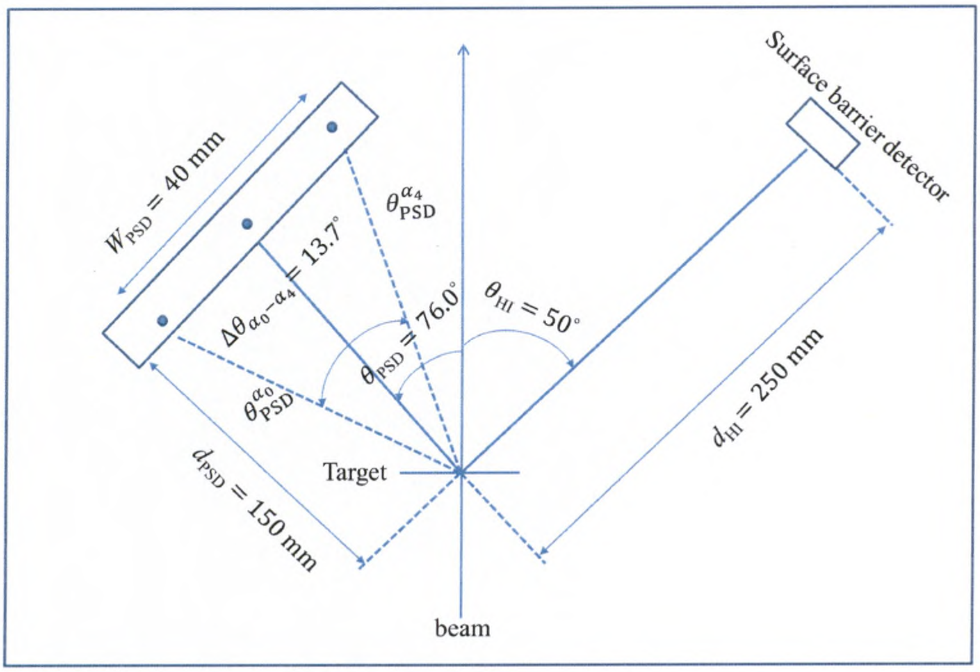

Figure 3.6: A typical kinematic coincidence set-up for ^{6}Li + ^{10}B at $\theta_{c.m.} \approx 90°$.

Table 3.1: The various kinematic quantities for the reaction $^{10}B(^{6}Li,\alpha_n)^{12}C^*(J^{\pi}, E_x)$ calculated using the kinematics programme CATKIN [CAT05].

$^{10}B(^{6}Li,\alpha_n)^{12}C^*(J^{\pi}, E_x)$ E_{Lab} = 18.143 MeV						
α_n	J^{π}	E_x (MeV)	$\theta_{PSD}(\alpha_n)$	$E_{PSD}(\alpha_n)$ (MeV)	$\theta_{HI}(^{12}C)$	$E_{HI}(^{12}C)$ (MeV)
α_0	0_1^+	0.000	−79.7°	26.972	+50°	14.884
α_1	2_1^+	4.430	−76.0°	24.365	+50°	13.061
α_2	0_2^+	7.650	−72.7°	22.542	+50°	11.682
α_3	3_1^-	9.640	−70.3°	21.416	+50°	10.800
α_4	1_1^+	12.710	−66.0°	19.767	+50°	9.379

3.4 Electronics diagram, data acquisition and detectors

The block diagram shown in Fig. 3.7 illustrates the electronics of the data acquisition system used in the experiments. The data acquisition system consists of three charge-sensitive preamplifiers (E_{HI}, POS_{PSD}, and E_{PSD}). In addition, there are three shaping spectroscopy amplifiers feeding the Timing Single Channel Analysers (TSCA's) triggering events on the analog to digital converters of the CAMAC system. The analog-to-digital converters (ADCs) had 2 μs with respect to the start of the strobe signal 14 μs wide while the delay amplifiers were used for timing and identification purposes.

Spectroscopy amplifiers from POS_{PSD} and E_{PSD} were fed into the position sensitive detector analyser module. Following which either the E_{PSD} output or the E_{HI} signal was used to indicate a valid event for generation of the ADCs strobe signal. The three signals E_{HI}, POS_{PSD} and E_{PSD}, brought into time coincidence, were processed by the CAMAC system using the WIMPS OS/2 programme for online data collection and extraction [FEA92]. The analog-to-digital converter outputs of the CAMAC system were stored in buffers of the online computer to be used for the display of various spectra. Figures for this section are placed at the end of the section for ease of reference.

3.4.1 Principles and operation of the silicon surface-barrier detectors used

There are different types of Position Sensitive Detectors (PSD), but in this experiment only an ORTEC solid state PSD was used. The ORTEC PSD is an n-type rectangular silicon surface-barrier detector, ion implanted on the front contact. The front contact is known as the p-n junction for this particular detector. There are four contacts for the signal extraction from the PSD detector. Two are the ohmic contacts providing the POS_{PSD} and E_{PSD} peak out from the detector while the other two are endpoints from the front contact. Typically, one of the two endpoints provides a signal whose height is proportional to the distance from the delay amplifier endpoint of the detector surface.

Figure 3.8 shows a typical experimental configuration for the PSD which allows for the simultaneous processing of the energy of the incoming particle and the position of the interaction of the incoming particle on the detector. As indicated in the diagram, a single bias for the detector is supplied through the preamplifier measuring the E_T (total energy signal). Two input signals from the main shaping amplifiers are needed for Position Sensitive Detector Analyser (ORTEC 464) to perform the position analysis function.

The silicon surface barrier detector used is a large area diode which consists of thin p-type layer on the sensitive face of a high purity and n-type silicon wafer. The two electrical contacts to the diode are of two types

- p-type surface through a gold thin film is approximately 40 μg/cm^2 thick, and
- through a non-rectifying metal contact to n-type silicon on the back surface.

A schematic diagram is shown in Fig. 3.9, in this illustration, D is the effective diameter corresponding to the active area of the device, L is the total thickness of the silicon wafer and W is the depth of the depletion region. The layer W corresponds to the portion of the silicon that contains an electric field resulting from external applied bias (V_b) on the diode. Free charges created in this layer by ionising radiation are separated under the influence of the electric field.

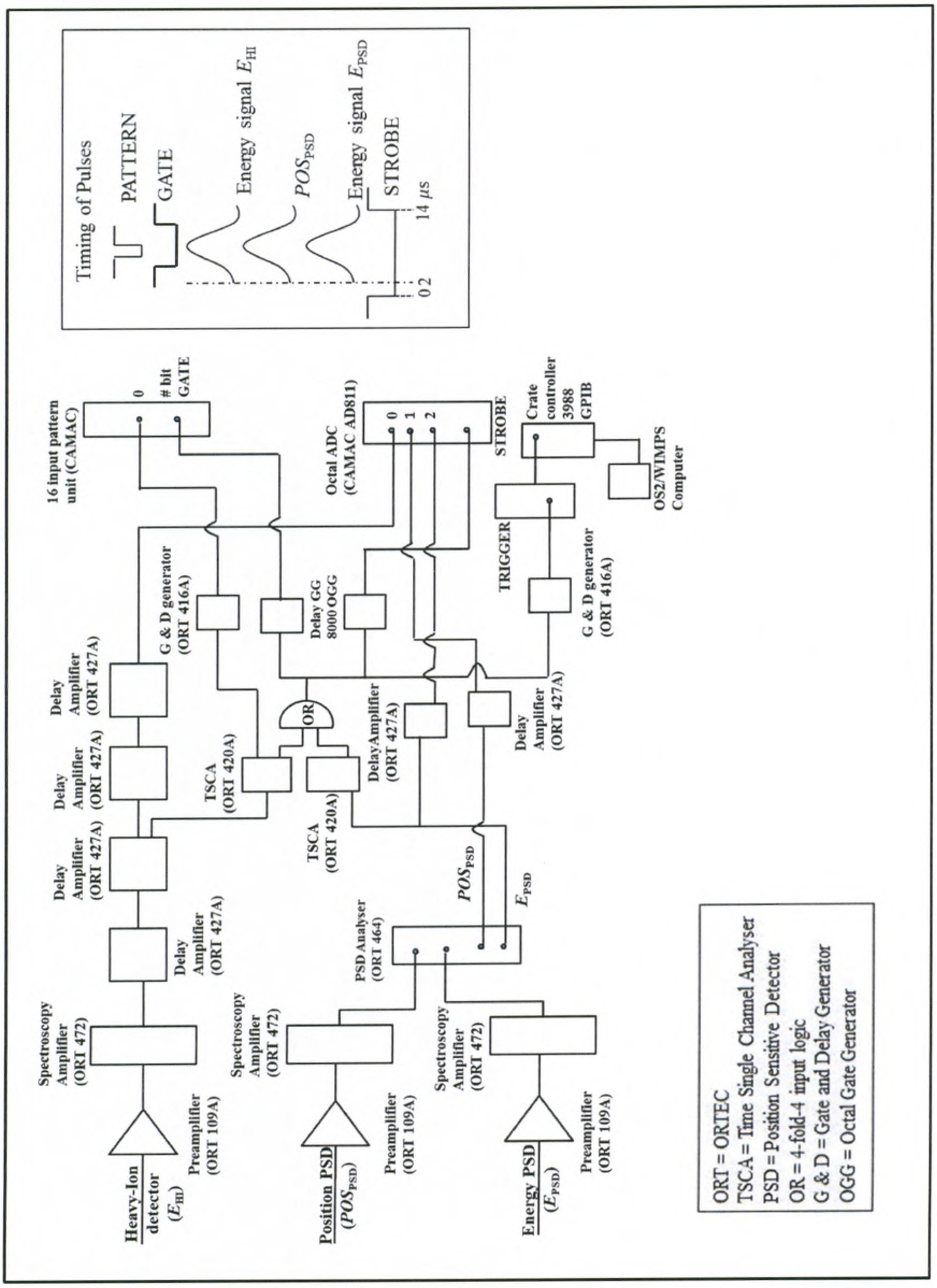

Figure 3.7: Electronics diagram and input to data acquisition system.

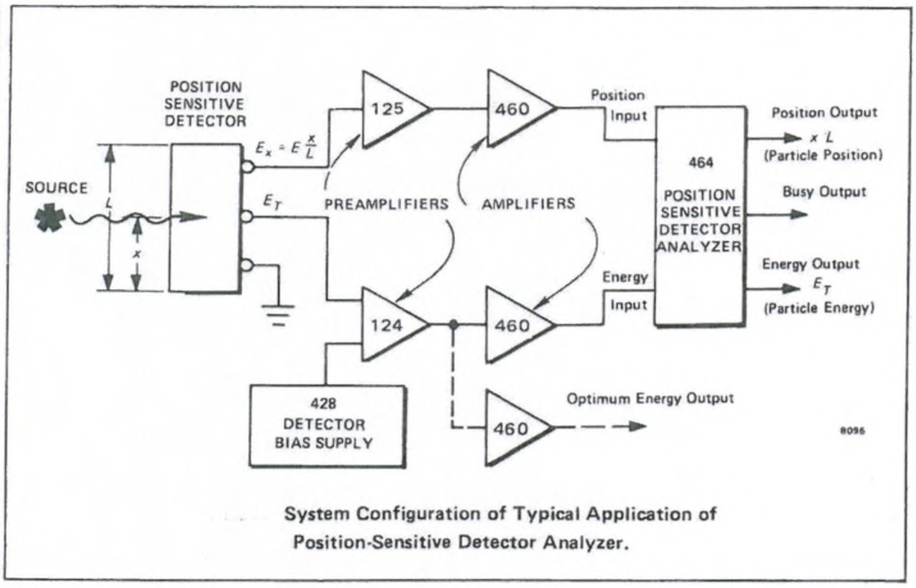

System Configuration of Typical Application of Position-Sensitive Detector Analyzer.

Figure 3.8: Schematic typical application of the Position Sensitive Detector [ORT74].

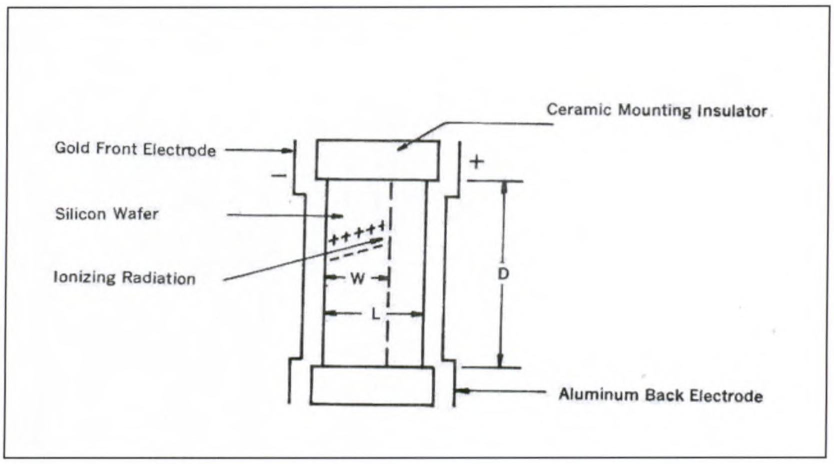

Figure 3.9: Schematic of a typical surface barrier detector [ORT68].

CHAPTER 4

Experimental results, analysis and discussion

Following the set-up of the kinematics coincidence system between the silicon position sensitive detector and the silicon singles detector described in Chapter 3, a calibration and linearity check was performed using elastic scattering of ^{12}C + ^{12}C as described in Section 4.1 below. This allowed for energy calibration of the singles detector prior to the measurement of the reaction ^{10}B (^{6}Li, α_n) ^{12}C which is presented in Section 4.2. In order to gain some insight into the change in yield of (^{6}Li, α) reaction, a preliminary angular distribution measurement was performed and is described in Section 4.3. Results of these measurements are discussed in Section 4.4.

4.1 Calibration of kinematic coincidence system using ^{12}C + ^{12}C elastic scattering

In order to ensure the correct functioning and set-up of the kinematic coincidence system described in Chapter 3, a sequence of measurements were taken using ^{12}C + ^{12}C elastic scattering at a conveniently available incident energy of E_{Lab} = 22.5 MeV. The resulting energy spectra are displayed in Figs. 4.1 – 4.7. For ease of reference, all of the figures in this section are placed at the end of the section.

A standard figure lay-out is shown in Fig. 4.1 where the top left panel shows the two-dimensional energy spectrum with the Position Sensitive Detector (PSD) along the x-axis, the Heavy-Ion (HI) detector along the y-axis and the time coincidence events distributed inside the two-dimensional matrix.

Since the elastic scattering of the identical particles requires the angle between the scattered and the recoil particle to be 90°, the HI detector when placed at

$\theta_{\text{Lab}}^{\text{HI}}$ = +30° requires the centre of the PSD to be positioned at $\theta_{\text{Lab}}^{\text{PSD}} = -60°$ with respect to the beam direction (see detector layout in Fig. 3.5). The corresponding energy spectrum for the HI detector is displayed in the middle right panel. As a starting point, the signals from the PSD position output determined by the PSD electronic module 464 A (see Fig. 3.7) are processed with the HI detector energy. To isolate the kinematic coincidence events of interest, a software gated region is defined in the two dimensional spectrum, seen as a rectangular box in the top left panel of Fig. 4.1. Projection down onto the x-axis of the events in this box yields the position spectrum of the PSD, POS_{PSD}, shown in the lower left panel and across onto the y-axis yields the energy spectrum of the HI detector, E_{HI}, shown in the lower right panel. By adjusting the gains of the main amplifiers for the energy and the position signals of the PSD, the resulting peak position can be placed in the middle of the POS_{PSD} spectrum, as seen in the lower left panel of Fig. 4.1, as a filled-in red peak. This corresponds to the physical position on the PSD in the middle of the detector. The recoil ^{12}C nucleus related to the scattered ^{12}C target at $\theta_{\text{Lab}}^{\text{HI}}$ = +30° is shown in the lower right panel, filled-in red peak, of Fig. 4.1. Here, it should be noted that the peak in the HI detector coincidence spectrum, lower right panel of Fig. 4.1, is located at the top end of the spectrum after adjusting the gain of the HI detector main amplifier. This was required since the energy of the scattered ^{12}C is at a maximum at the most forward scattering angle $\theta_{\text{Lab}}^{\text{HI}}$ = +30°.

With the required amplifier and timing settings having been made, a series of measurements were taken for various scattering angles $\theta_{\text{Lab}}^{\text{HI}}$ = +30°, +35°, +40°, +45°, +50°, +55°, the results of which are shown in Figs. 4.2 – 4.7, respectively. As can be seen, the red rectangular box moves down and across the two-dimensional spectrum, upper left panel in each figure, following the increase of the $\theta_{\text{Lab}}^{\text{HI}}$ angle. In addition, with the corresponding decrease of the $\theta_{\text{Lab}}^{\text{PSD}}$ angle, it can be seen that the peak position of E_{PSD} increases as shown in the left lower panel in Figs. 4.2 – 4.7, respectively. Also, it was checked that the gains of the main amplifiers for the energy and position signals of PSD yielded an energy coincidence peak, E_{PSD}, at the top end of the energy spectrum for the most forward scattering angle of the PSD, $\theta_{\text{Lab}}^{\text{PSD}} = -35°$ (see Fig. 4.7).

The corresponding peak positions for E_{PSD} and E_{HI} were determined from the coincidence energy spectra and are given in Table 4.1. It is then possible to obtain energy calibration curves for the HI and PSD detectors. These are shown in Fig. 4.8 for each detector with the corresponding linear regression straight-line fits to the data. The fits confirm linearity of the two detectors and indicate an acceptable close to zero intercept on the x-axis.

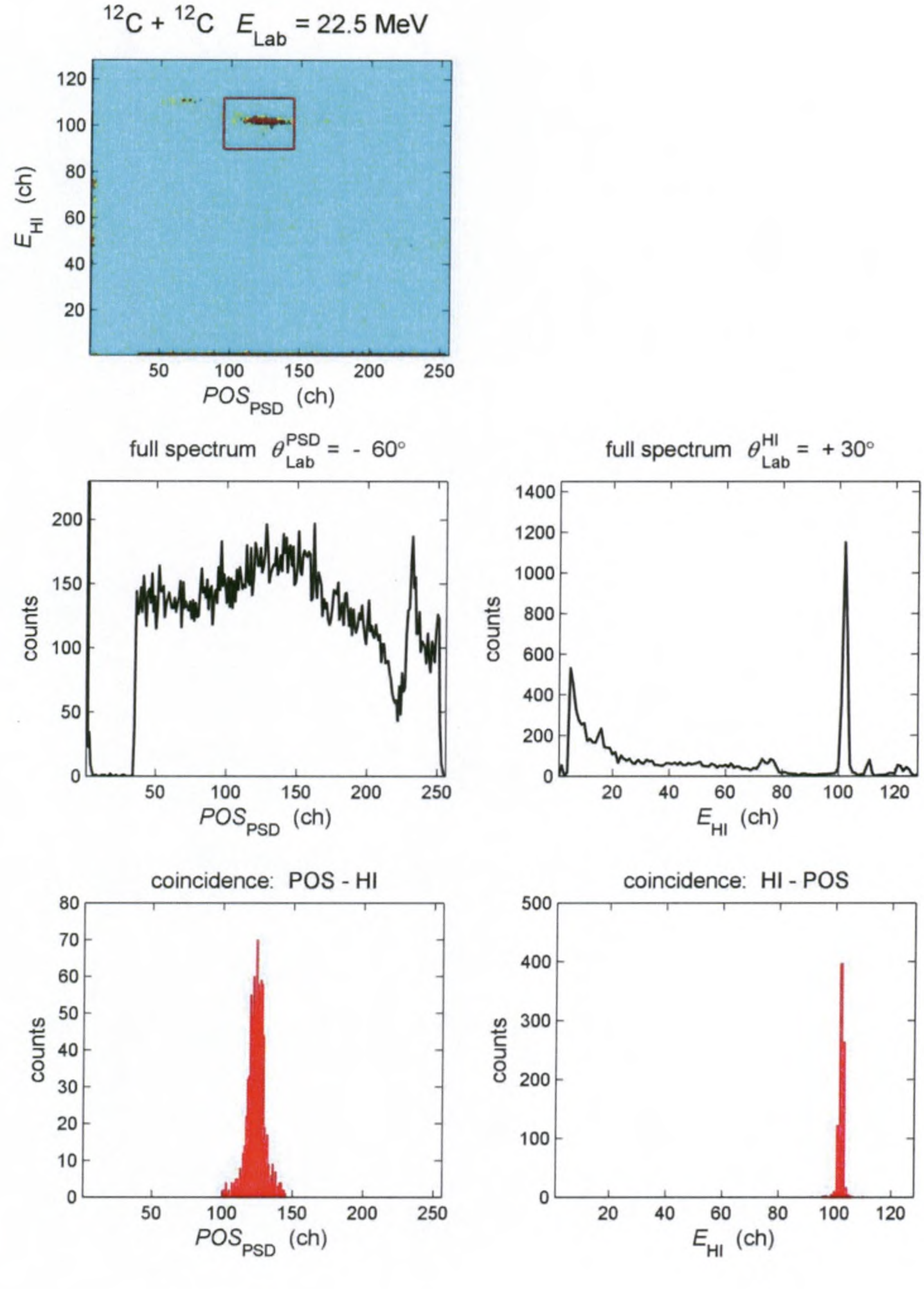

Figure 4.1: Calibration spectra for POS_{PSD} and E_{HI} at θ^{HI}_{Lab} = +30°. The red shaded peaks in the lower spectra indicate the ^{12}C + ^{12}C elastic scattering coincidence between the PSD and HI detectors at the scattering angles indicated, $\theta^{PSD}_{Lab} = -60°$ and $\theta^{HI}_{Lab} = +30°$.

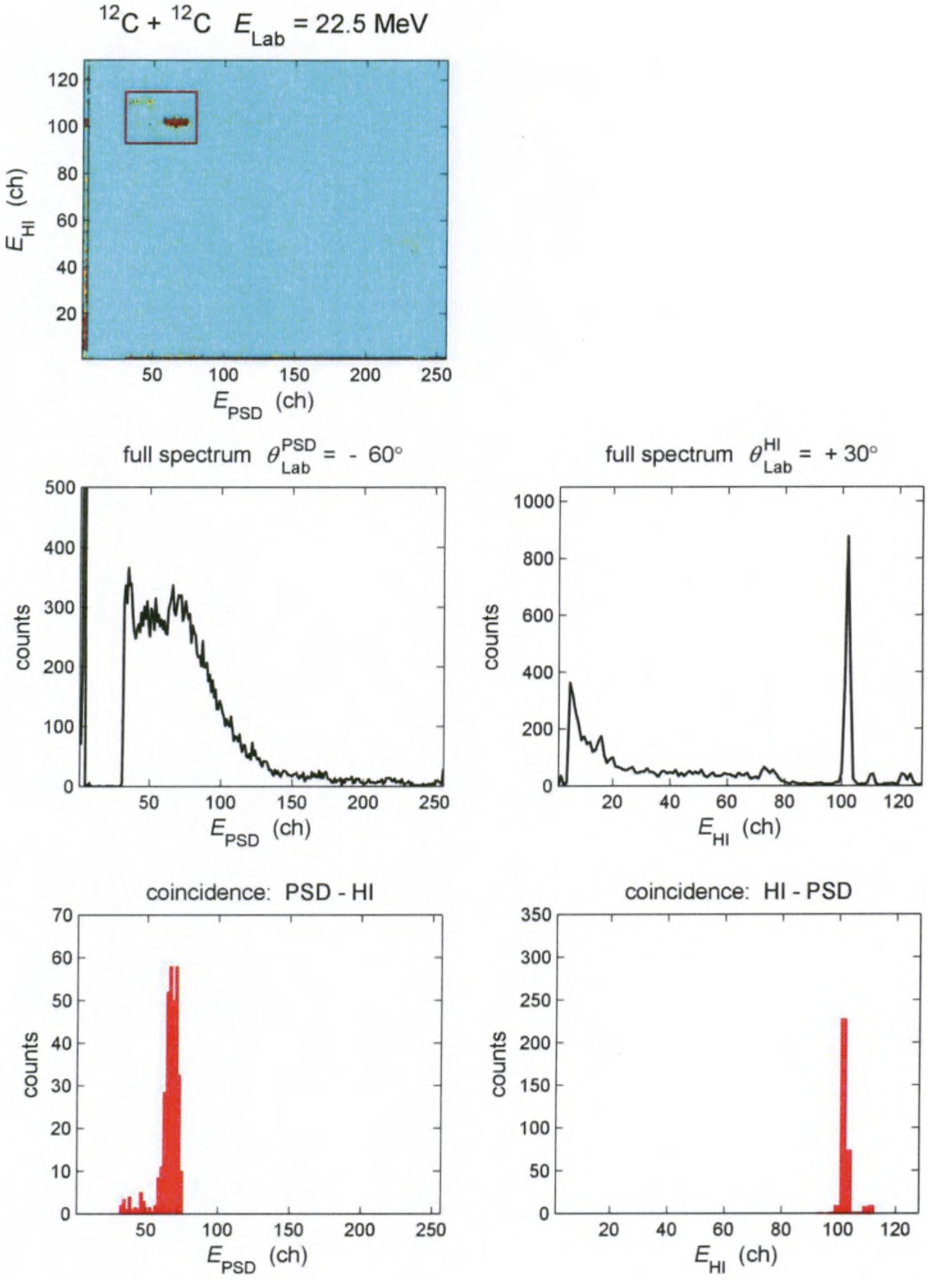

Figure 4.2: Calibration spectra for E_{PSD} and E_{HI} at θ_{Lab}^{HI} = +30°. The red shaded peaks in the lower spectra indicate the ^{12}C + ^{12}C elastic scattering coincidence between the PSD and HI detectors at the scattering angles indicated, θ_{Lab}^{PSD} = −60° and θ_{Lab}^{HI} = +30°.

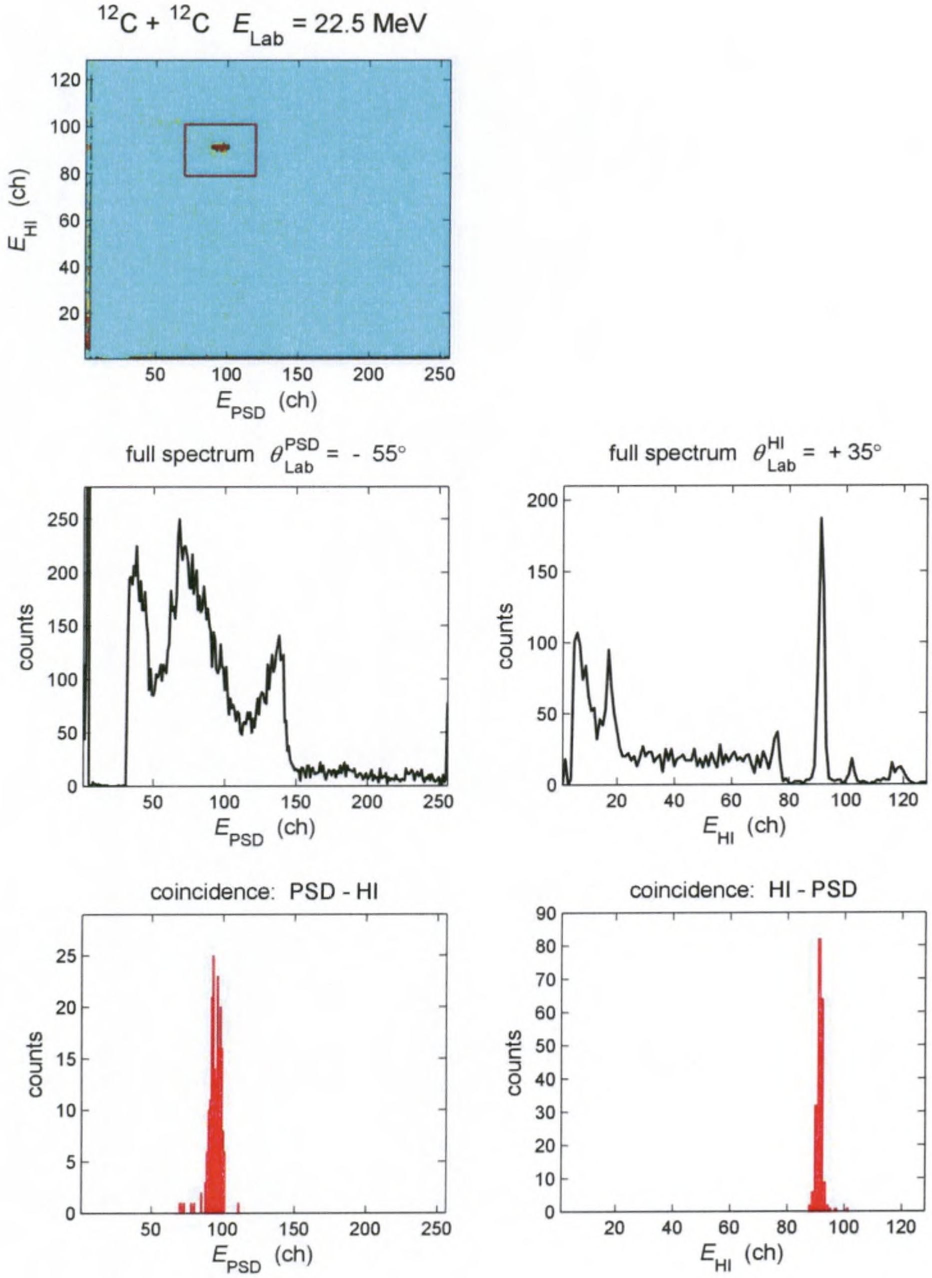

Figure 4.3: Calibration spectra for E_{PSD} and E_{HI} at $\theta^{\mathrm{HI}}_{\mathrm{Lab}} = +35^{\circ}$. The red shaded peaks in the lower spectra indicate the ^{12}C + ^{12}C elastic scattering coincidence between the PSD and HI detectors at the scattering angles indicated, $\theta^{\mathrm{PSD}}_{\mathrm{Lab}} = -55^{\circ}$ and $\theta^{\mathrm{HI}}_{\mathrm{Lab}} = +35^{\circ}$.

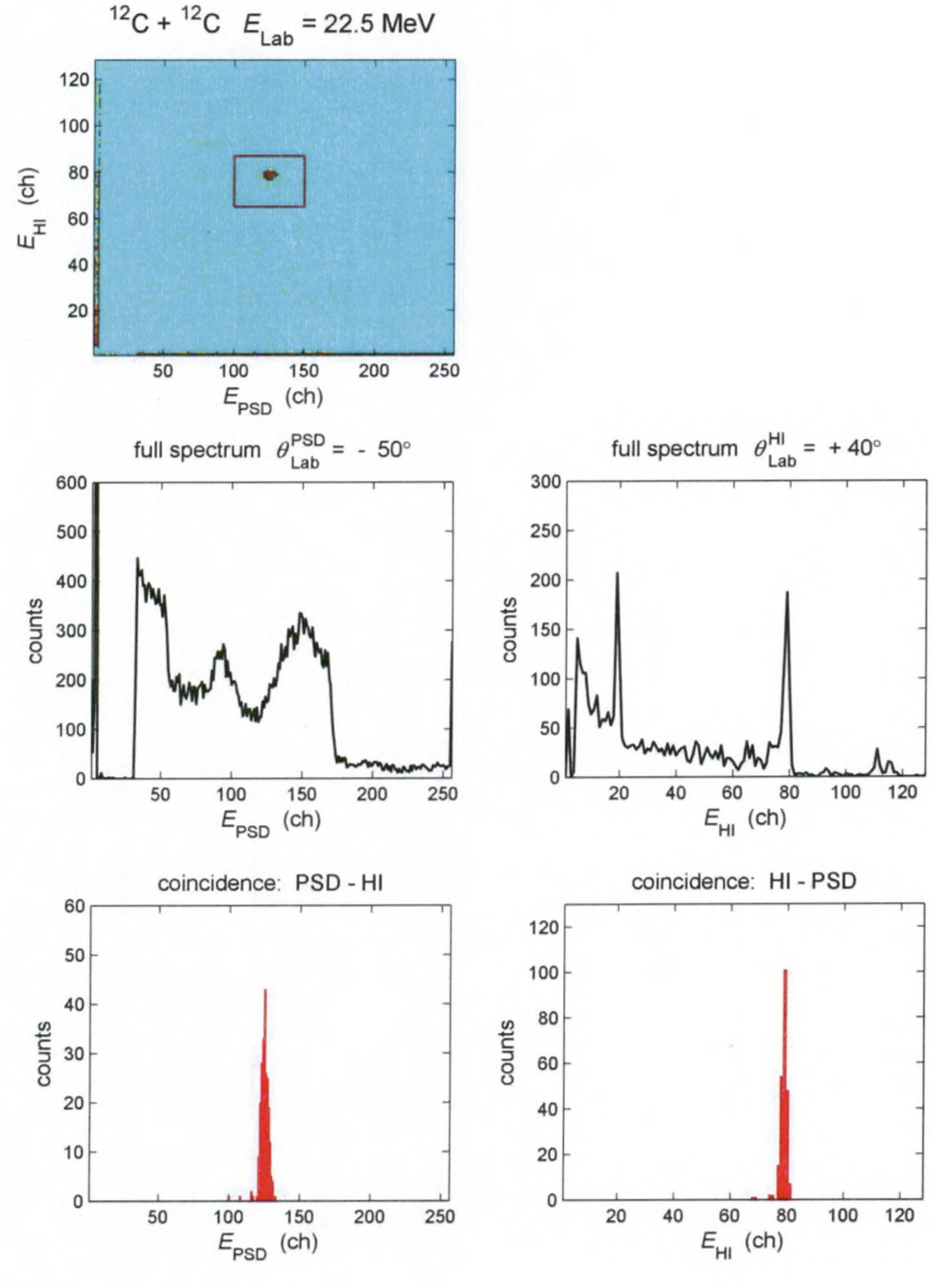

Figure 4.4: Calibration spectra for E_{PSD} and E_{HI} at θ^{HI}_{Lab} = +40°. The red shaded peaks in the lower spectra indicate the $^{12}C + ^{12}C$ elastic scattering coincidence between the PSD and HI detectors at the scattering angles indicated, $\theta^{PSD}_{Lab} = -50°$ and θ^{HI}_{Lab} = +40°.

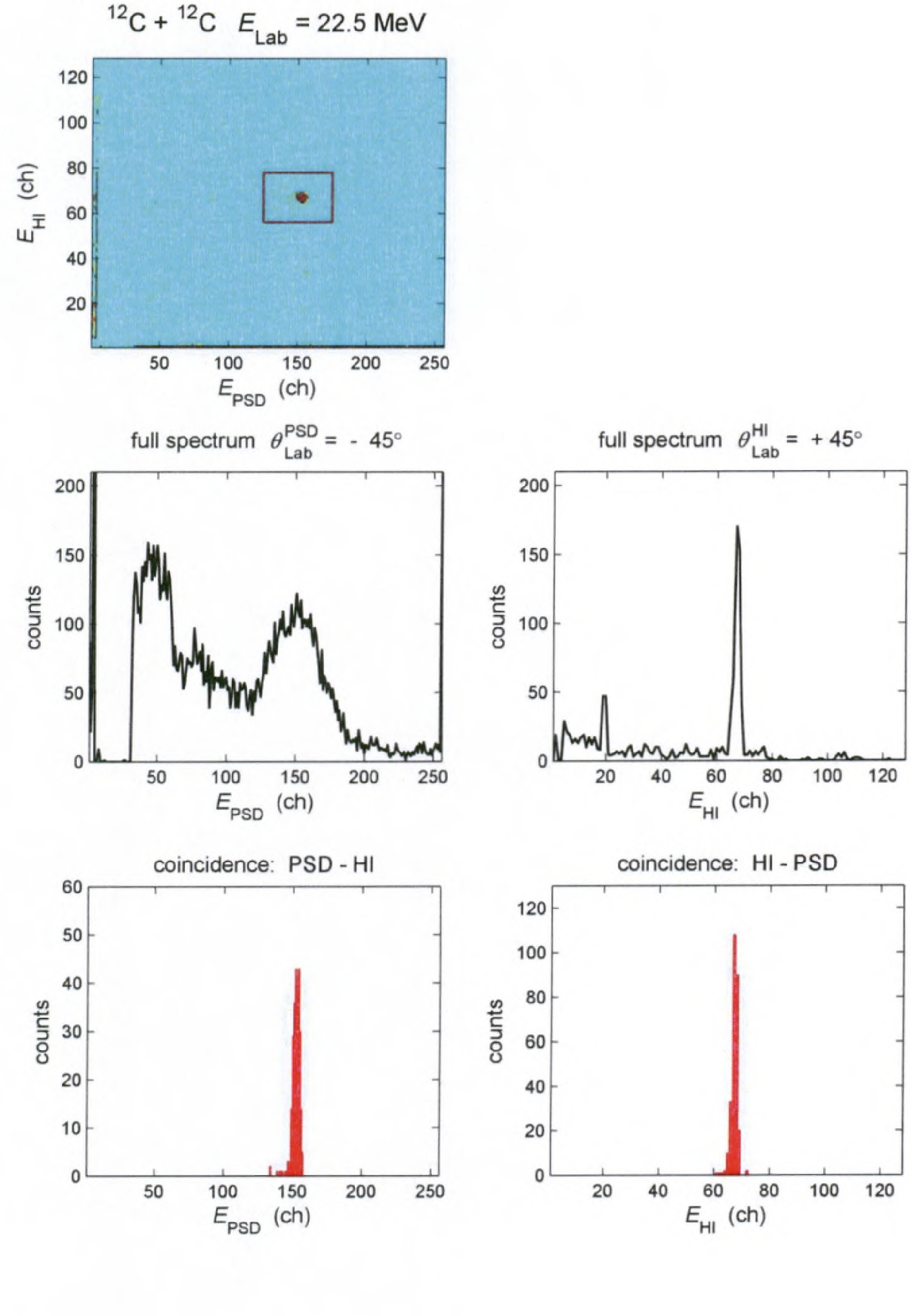

Figure 4.5: Calibration spectra for E_{PSD} and E_{HI} at $\theta^{\text{HI}}_{\text{Lab}} = +45^{\circ}$. The red shaded peaks in the lower spectra indicate the $^{12}\text{C} + ^{12}\text{C}$ elastic scattering coincidence between the PSD and HI detectors at the scattering angles indicated, $\theta^{\text{PSD}}_{\text{Lab}} = -45^{\circ}$ and $\theta^{\text{HI}}_{\text{Lab}} = +45^{\circ}$.

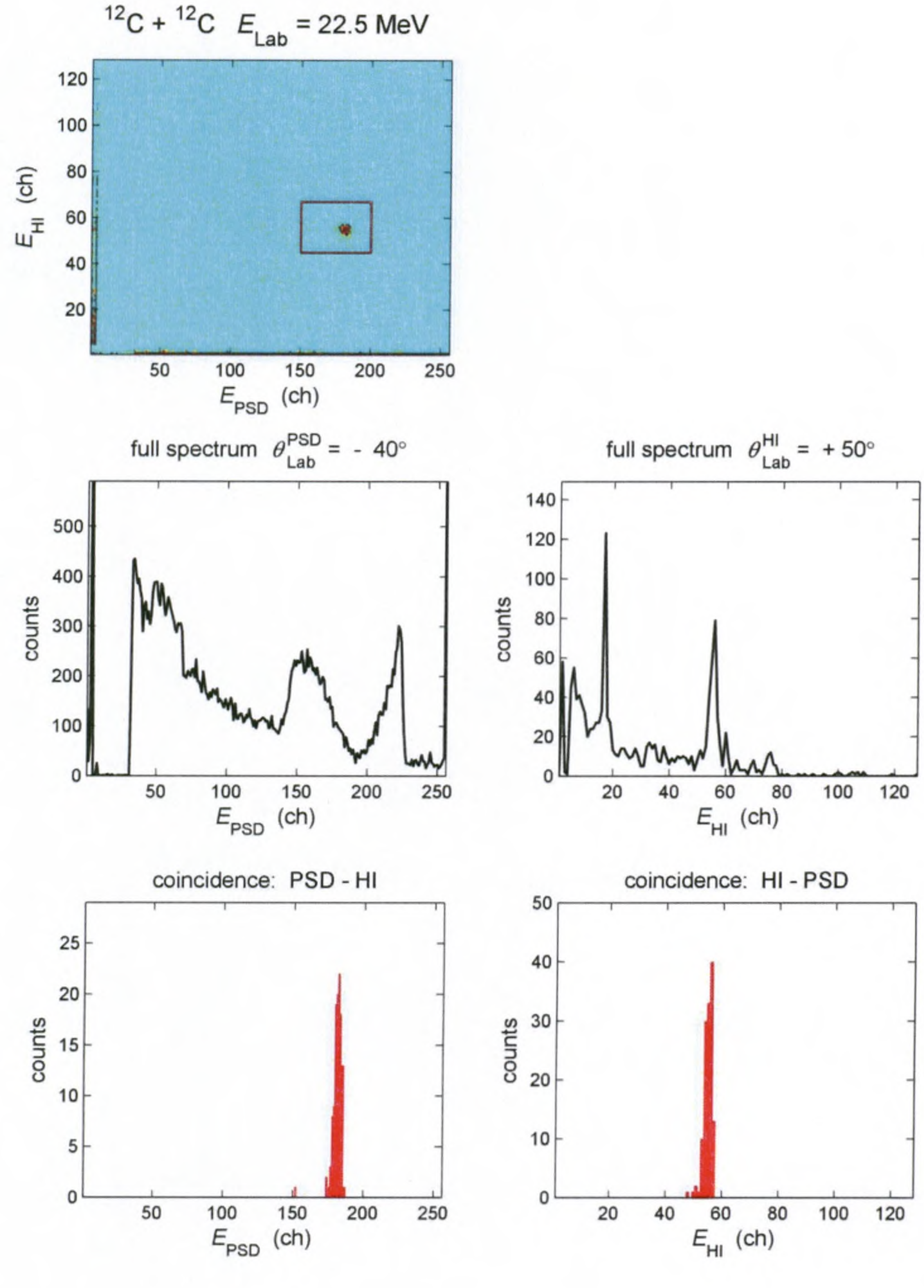

Figure 4.6: Calibration spectra for E_{PSD} and E_{HI} at $\theta_{\text{Lab}}^{\text{HI}} = +50^{\circ}$. The red shaded peaks in the lower spectra indicate the ^{12}C + ^{12}C elastic scattering coincidence between the PSD and HI detectors at the scattering angles indicated, $\theta_{\text{Lab}}^{\text{PSD}} = -40^{\circ}$ and $\theta_{\text{Lab}}^{\text{HI}} = +50^{\circ}$.

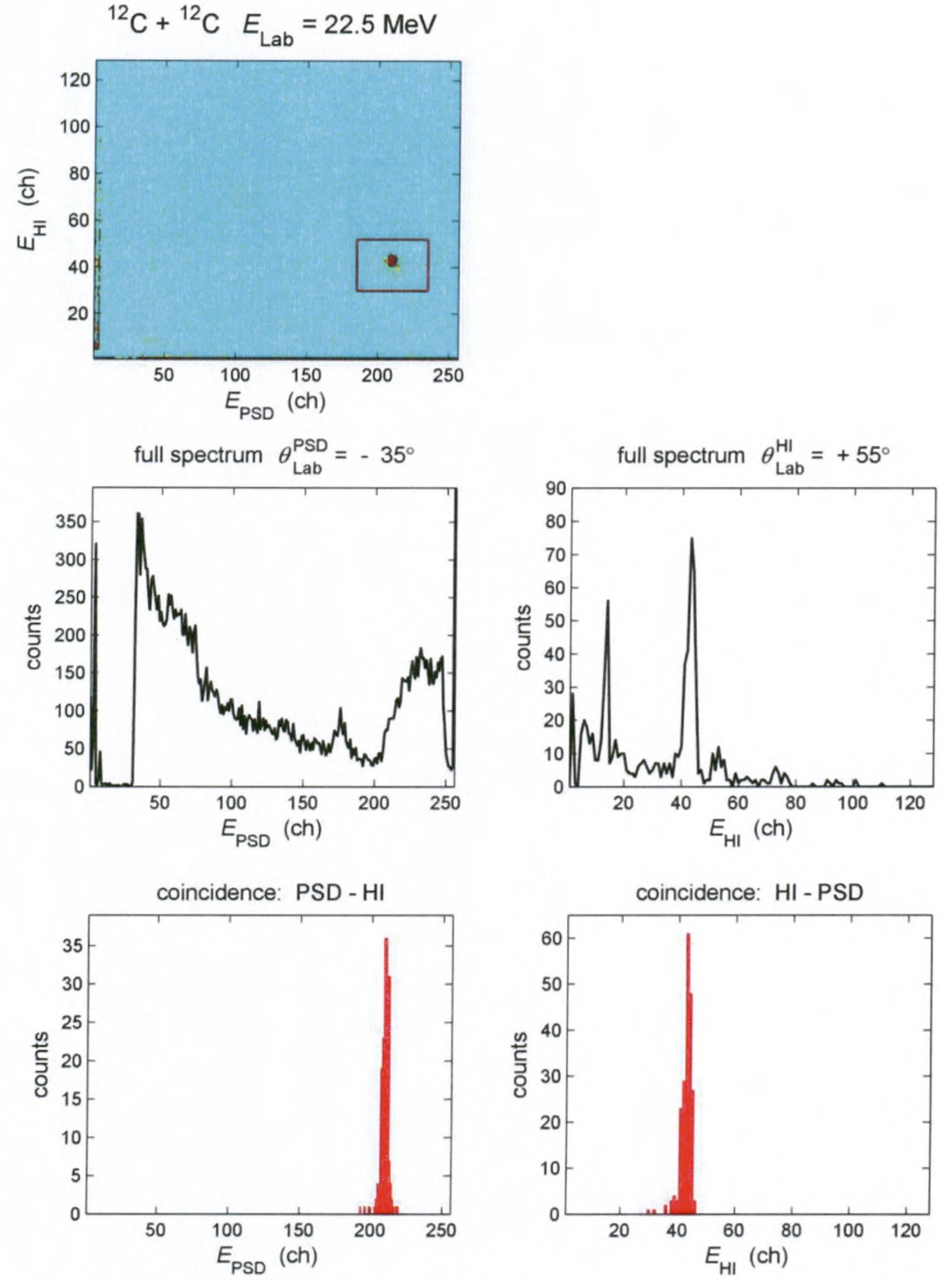

Figure 4.7: Calibration spectra for E_{PSD} and E_{HI} at θ^{HI}_{Lab} = +55°. The red shaded peaks in the lower spectra indicate the $^{12}C + ^{12}C$ elastic scattering coincidence between the PSD and HI detectors at the scattering angles indicated, $\theta^{PSD}_{Lab} = -35°$ and θ^{HI}_{Lab} = +55°.

Table 4.1: The kinematic coincidence of $^{12}C + ^{12}C$ at $E_{Lab} = 22.5$ MeV.

$^{12}C + ^{12}C$ $E_{Lab} = 22.5$ MeV					
θ_{PSD}	θ_{HI}	E_{PSD} (MeV)	E_{PSD} (ch)	E_{HI} (MeV)	E_{HI} (ch)
−60°	+30°	5.625	72.0	16.875	102.5
−55°	+35°	7.402	98.0	15.098	90.5
−50°	+40°	9.296	128.0	13.204	78.5
−45°	+45°	11.250	150.5	11.250	66.5
−40°	+50°	13.204	186.5	9.296	54.5
−35°	+55°	15.098	210.5	7.402	42.5

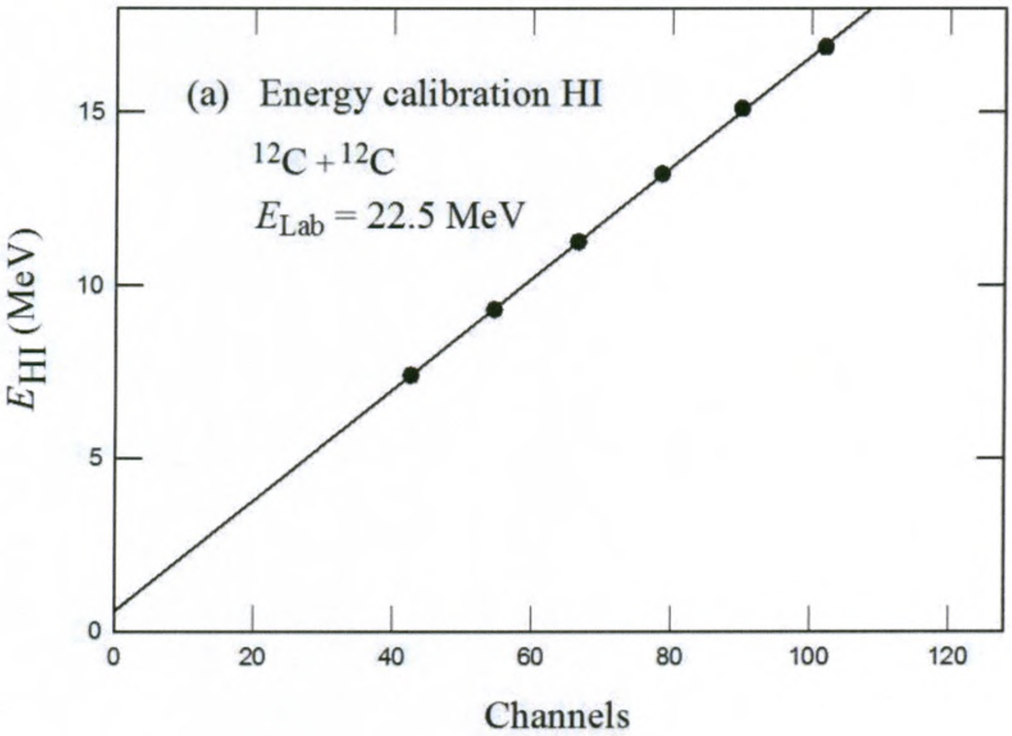

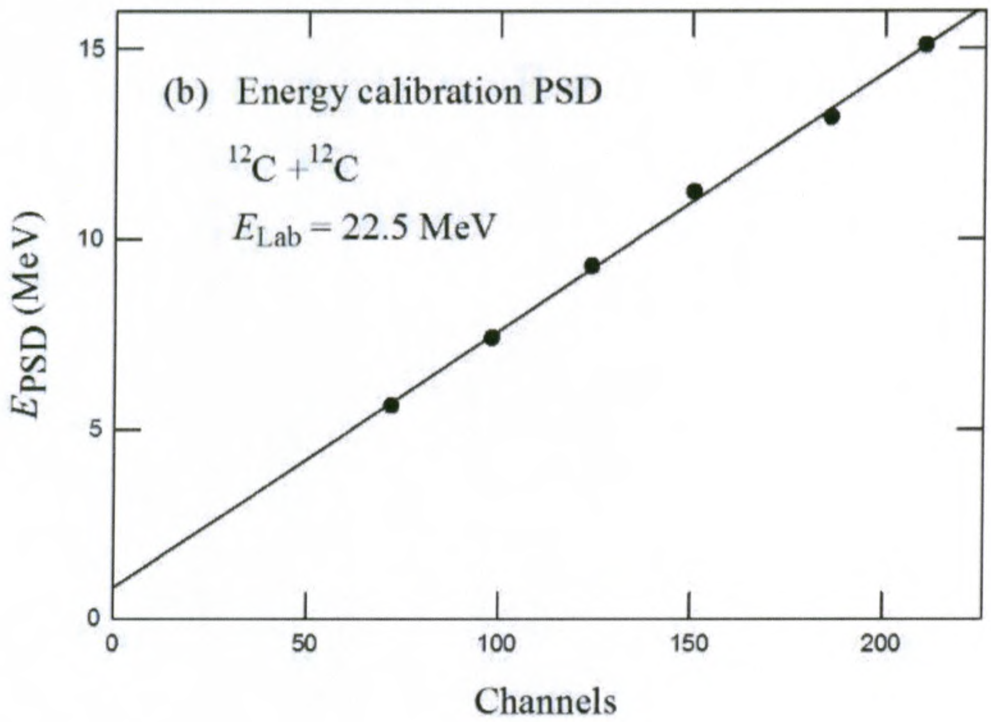

Figure 4.8: Energy calibration for $^{12}C + ^{12}C$ at E_{Lab} = 22.5 MeV (a) heavy-ion detector and (b) position sensitive detector.

4.2 Measurement of the $^{10}B\ (^{6}Li,\alpha_n)^{12}C^*\ (J^{\pi}, E_x)$ reaction

Following the successful commissioning of the kinematic coincidence system, the $^{10}B\ (^{6}Li,\alpha_n)^{12}C^*\ (J^{\pi}, E_x)$ reaction was measured at the highest available incident beam energy $E_{Lab}\ (^{6}Li) = 18.143$ MeV. Noting that the ground state Q-value of the reaction is fairly large, $Q_{g.s.} = 23.713$ MeV, the reaction produces α-particles in the energy range $E_{\alpha} \approx 20$ - 30 MeV depending upon the scattering angle chosen for the measurement. An extended measurement of 8 hours was performed for a steady beam current of $I\ (^{6}Li^{3+}) \approx 6$ enA with the HI detector placed at $\theta^{HI}_{Lab} = +50^{o}$ which allowed for the detection of the $^{12}C\ (0^{+}$, g.s.) close to $E_{Lab}\ (^{12}C\ (0^{+}$, g.s.)) ≈ 15 MeV ranging to $^{12}C\ (1^{+}$, 12.710 MeV) at $E_{Lab}\ (^{12}C\ (1^{+}$, 12.71 MeV)) $\approx$ 9 MeV, within the capability of the HI detector as described in Section 4.1. The corresponding α-particle energies $\alpha_0 - \alpha_4$ range from 27 – 21 MeV at scattering angles within the angular acceptance of the PSD. This angle setting corresponds to a centre-of-mass scattering angle $\theta_{c.m.} \approx 90^{o}$. The sensitive depth of the PSD used and the corresponding maximum energy alpha-particle stopped were 500 microns and 35 MeV, repectively, requiring main amplifier gain adjustments during this part of the experimental work. The measured energy spectra are displayed in Fig. 4.9 and the corresponding reaction kinematics are summarised in Table 4.2. For ease of identification, the open black circles shown in the top left panel of Fig. 4.9 for the two dimensional E_{HI} *versus* E_{PSD} are labelled $\alpha_0 - \alpha_4$. Projection down onto the E_{PSD} axis produces the resulting coincidence E_{PSD} energy spectrum seen in the lower left panel of Fig. 4.9 while projection across to the E_{HI} axis results in the E_{HI} energy spectrum displayed in the lower right panel of Fig. 4.9. In order to guide the eye, Gaussian shaped peaks are plotted and labelled $\alpha_0 - \alpha_4$ (lower left panel Fig. 4.9) and correspondingly $^{12}C\ (0^{+}$, g.s.) and $^{12}C\ (2^{+}$, 4.43 MeV) (lower right panel Fig. 4.9). The filled red histogram indicates the coincidence measurement projections. As can be seen, the α_1 channel is the most strongly populated with limited counts appearing at the α_0 position. Using the calibration obtained from α_0 and α_1 the positions of α_3, α_4 and α_5 were then determined. Table 4.2 summarises the energy levels of ^{12}C populated by the reaction of $^{10}B\ (^{6}Li, \alpha_n)\ ^{12}C^*$, the values in red for E_{PSD} and E_{HI} are the data measured while those in green are the predicted values from the kinematic calculation and internal energy calibration of the detectors.

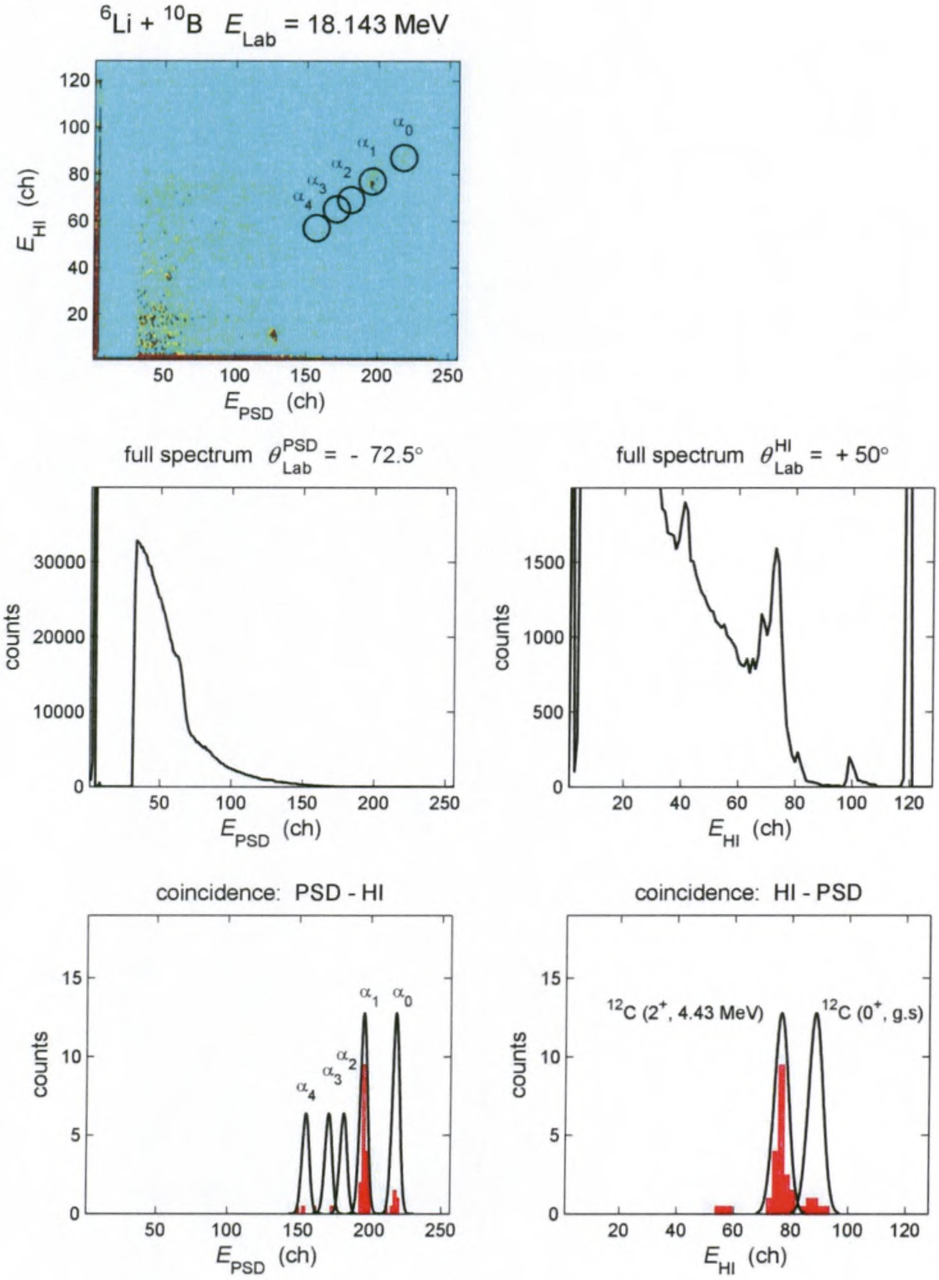

Figure 4.9: Measurement of the ^{10}B (^{6}Li, α_n) ^{12}C* reaction at E_{Lab} = 18.143 MeV corresponding to $\theta^{\text{HI}}_{\text{Lab}}$ = +50° and projections of α_n and ^{12}C.

Table 4.2: Energy levels of ^{12}C populated by the reaction $^{10}B(^{6}Li, \alpha_n)\,^{12}C^*$.

$^{10}B(^{6}Li,\alpha_n)^{12}C^*(J^\pi, E_x)$ E_{Lab} = 18.143 MeV								
α_n	J^π	E_x (MeV)	$\theta_{PSD}(\alpha_n)$	$E_{PSD}(\alpha_n)$ (MeV)	$E_{PSD}(\alpha_n)$ (ch)	$\theta_{HI}(^{12}C)$	$E_{HI}(^{12}C)$ (MeV)	$E_{HI}(^{12}C)$ (ch)
α_0	0_1^+	0.000	−79.7°	26.972	**218**	+50°	14.884	**87**
α_1	2_1^+	4.430	−76.0°	24.365	**196**	+50°	13.061	**77**
α_2	0_2^+	7.650	−72.7°	22.542	**181**	+50°	11.682	**69**
α_3	3_1^-	9.640	−70.3°	21.416	**171**	+50°	10.800	**65**
α_4	1_1^+	12.710	−66.0°	19.767	**157**	+50°	9.379	**57**

4.3 Preliminary angular distribution for $^{10}B(^{6}Li, \alpha_n)\,^{12}C^*$ at E_{Lab} = 20 MeV

As a follow-on from the measurement of $^{10}B(^{6}Li, \alpha_n)\,^{12}C^*$ taken at $\theta_{c.m.} \approx 90^o$ described in Section 4.2, a series of short runs were performed at various scattering angles $58^o \lesssim \theta_{c.m.} \lesssim 103^o$. These measurements should be regarded as preliminary to confirm the kinematic movement within the two-dimensional E_{HI} *versus* E_{PSD} plot and to determine changes in the population of states in ^{12}C, the results of which are presented in Figs. 4.10 – 4.13. It should be noted that the incident ^{6}Li beam energy was increased to E_{Lab} = 20 MeV and the measurement at E_{Lab} = 18.143 MeV for $\theta_{HI} = +50^o$ described in Section 4.2 was repeated. Here, the results of Fig. 4.11 should be compared with Fig. 4.9 where again the α_0 and α_1 channels can be identified in the projected coincidence spectrum (lower left panel). The region of the projection is shown by the rectangular box in the top left panel of Fig. 4.11. As can be seen from Fig. 4.10 ($\theta_{HI} = +40^o$, $\theta_{c.m.} \approx 103^o$) the kinematic projection rectangle moves from just past middle top right progressively down and across as in Fig. 4.11 ($\theta_{HI} = +50^o$, $\theta_{c.m.} \approx 90^o$) to Fig. 4.12 ($\theta_{HI} = +60^o$, $\theta_{c.m.} \approx 73^o$) to Fig. 4.13 ($\theta_{HI} = +70^o$, $\theta_{c.m.} \approx 58^o$). In all cases only the α_1 channel is populated strongly, with a correspondingly small yield to the α_0 channel. The maximum alpha-particle energy that can be detected at θ_{HI} = $+70^o$ is within the stopping range of the PSD (see Table 4.3).

Table 4.3 lists the calculated kinematic energies for the reaction $^{10}B(^{6}Li, \alpha_1)\,^{12}C$ (2_1^+, 4.43 MeV) at the respective kinematic coincidence settings. In order to obtain a preliminary guide to the change in cross-section for the α_1 channel as a function of centre-of-mass angle, Table 4.4 lists the yield to the α_1 channel subsequently normalised to counts / (hour enA), with the uncertainty in the yield for population of the α_1 channel ^{12}C (2_1^+) determined from the counting statistics and a 10% uncertainty on the average beam current.

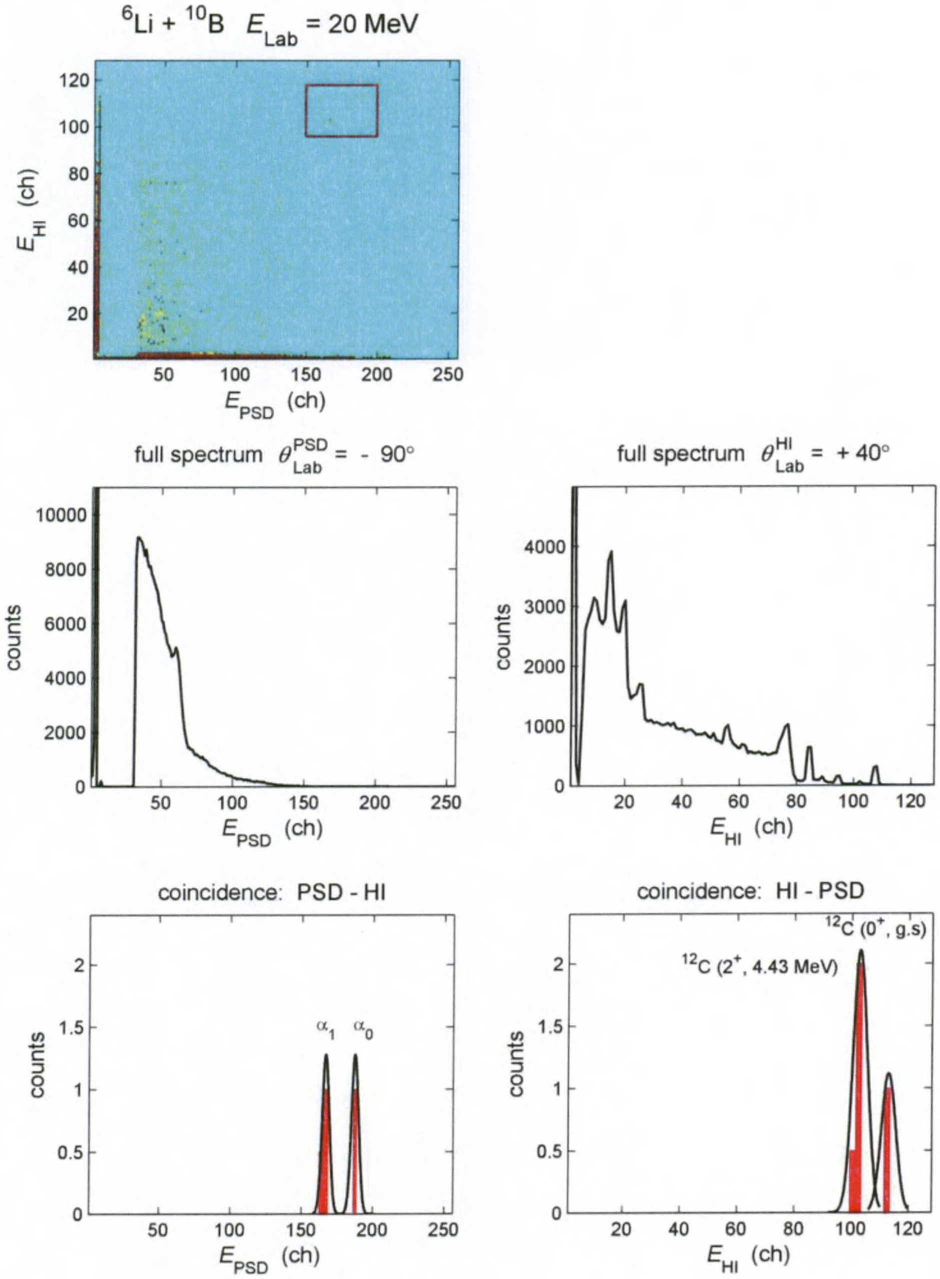

Figure 4.10: Preliminary angular distribution measurement for the ^{10}B (^{6}Li, α_n) ^{12}C* reaction at E_{Lab} = 20 MeV corresponding to $\theta_{\mathrm{Lab}}^{\mathrm{PSD}} = -90^{\circ}$ and $\theta_{\mathrm{Lab}}^{\mathrm{HI}} = +40^{\circ}$ with the projections of α_n and ^{12}C for the kinematic coincidence region indicated by the red rectangle in the upper left panel.

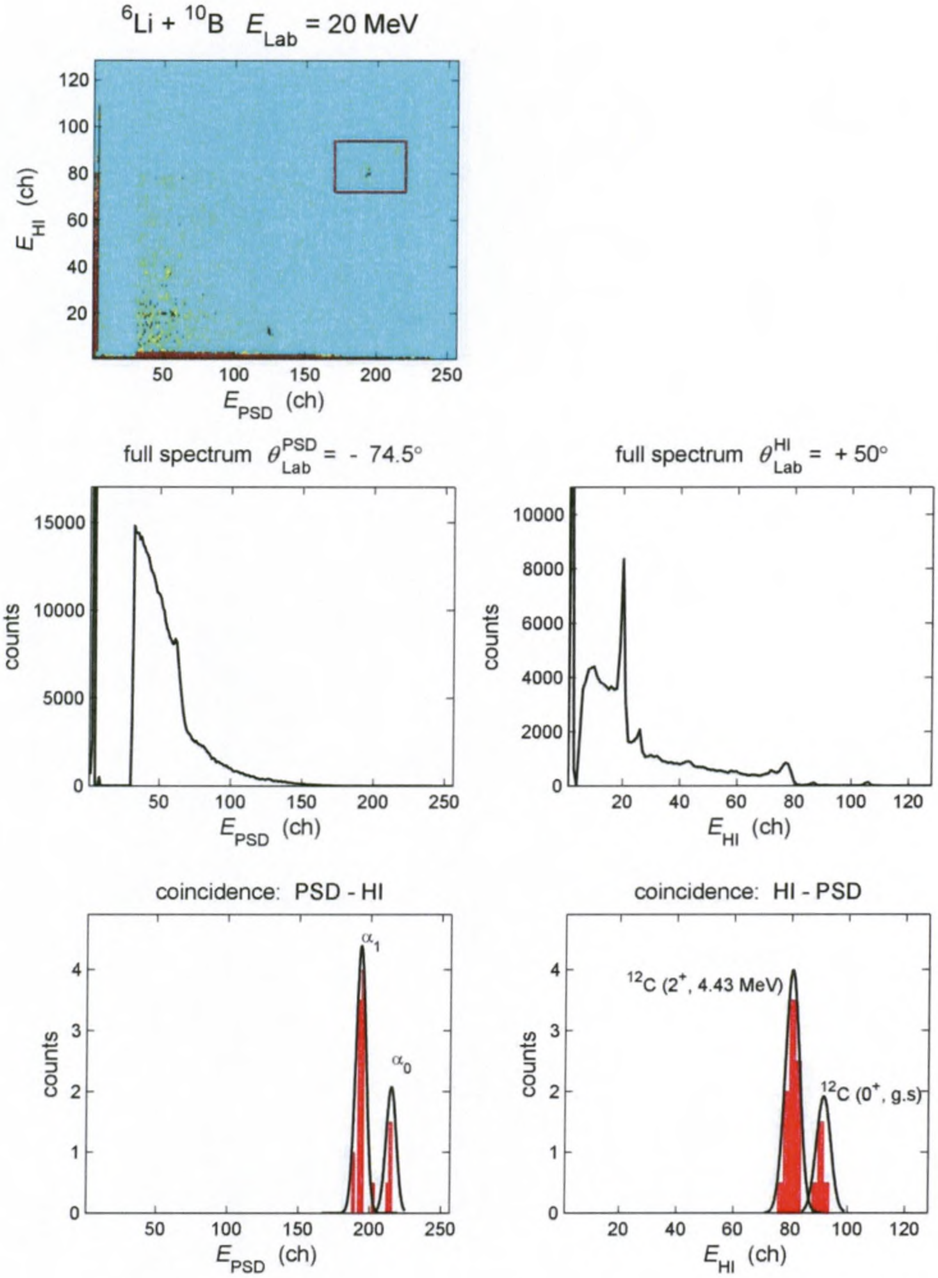

Figure 4.11: Preliminary angular distribution measurement for the ^{10}B (^{6}Li, α_n) ^{12}C* reaction at E_{Lab} = 20 MeV corresponding to $\theta_{\text{Lab}}^{\text{PSD}} = -74.5^{\circ}$ and $\theta_{\text{Lab}}^{\text{HI}} = +50^{\circ}$ with the projections of α_n and ^{12}C for the kinematic coincidence region indicated by the red rectangle in the upper left panel.

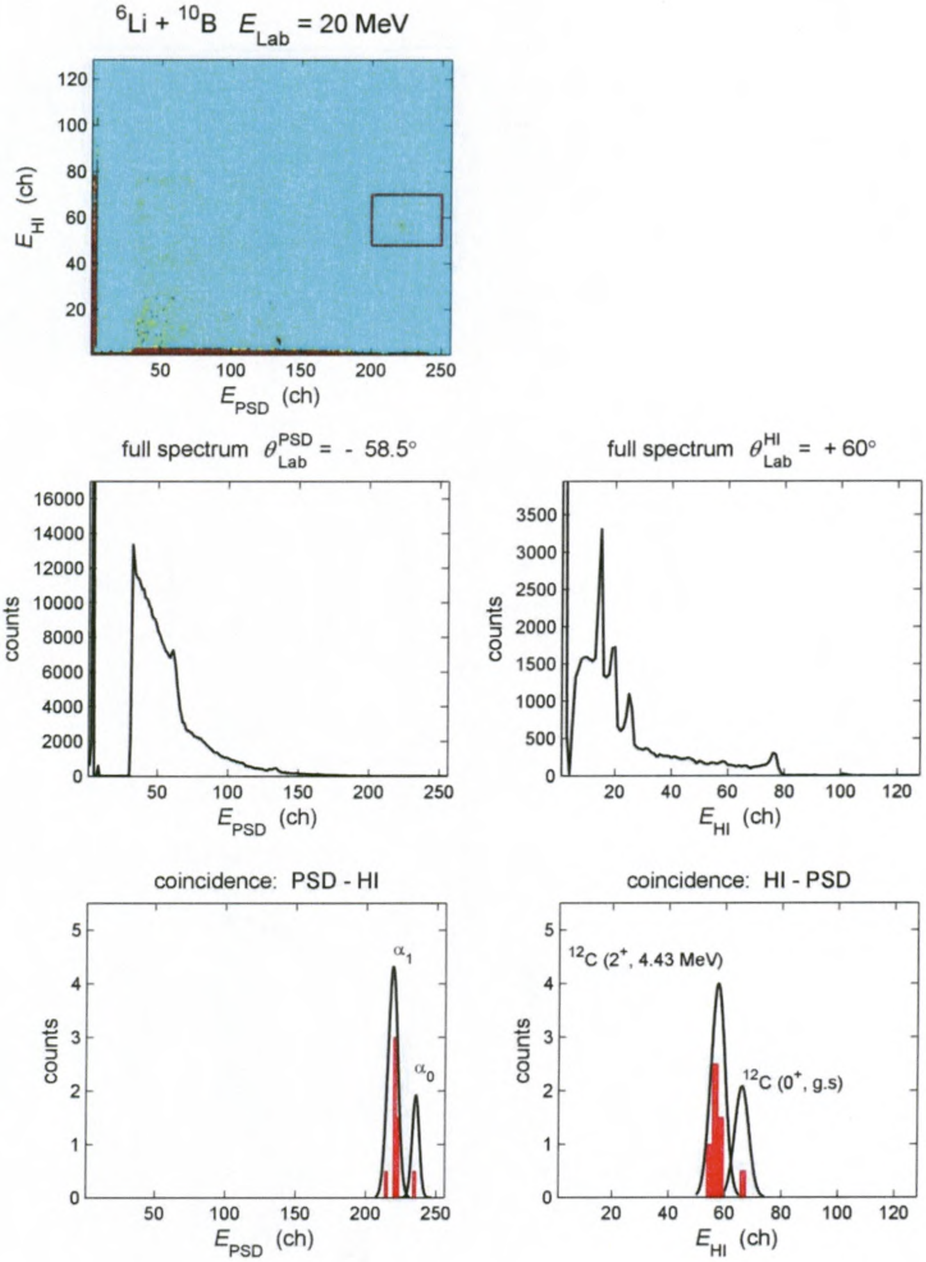

Figure 4.12: Preliminary angular distribution measurement for the ^{10}B (^{6}Li, α_n) ^{12}C* reaction at E_{Lab} = 20 MeV corresponding to $\theta_{\mathrm{Lab}}^{\mathrm{PSD}} = -58.5^{\circ}$ and $\theta_{\mathrm{Lab}}^{\mathrm{HI}} = +60^{\circ}$ with the projections of α_n and ^{12}C for the kinematic coincidence region indicated by the red rectangle in the upper left panel.

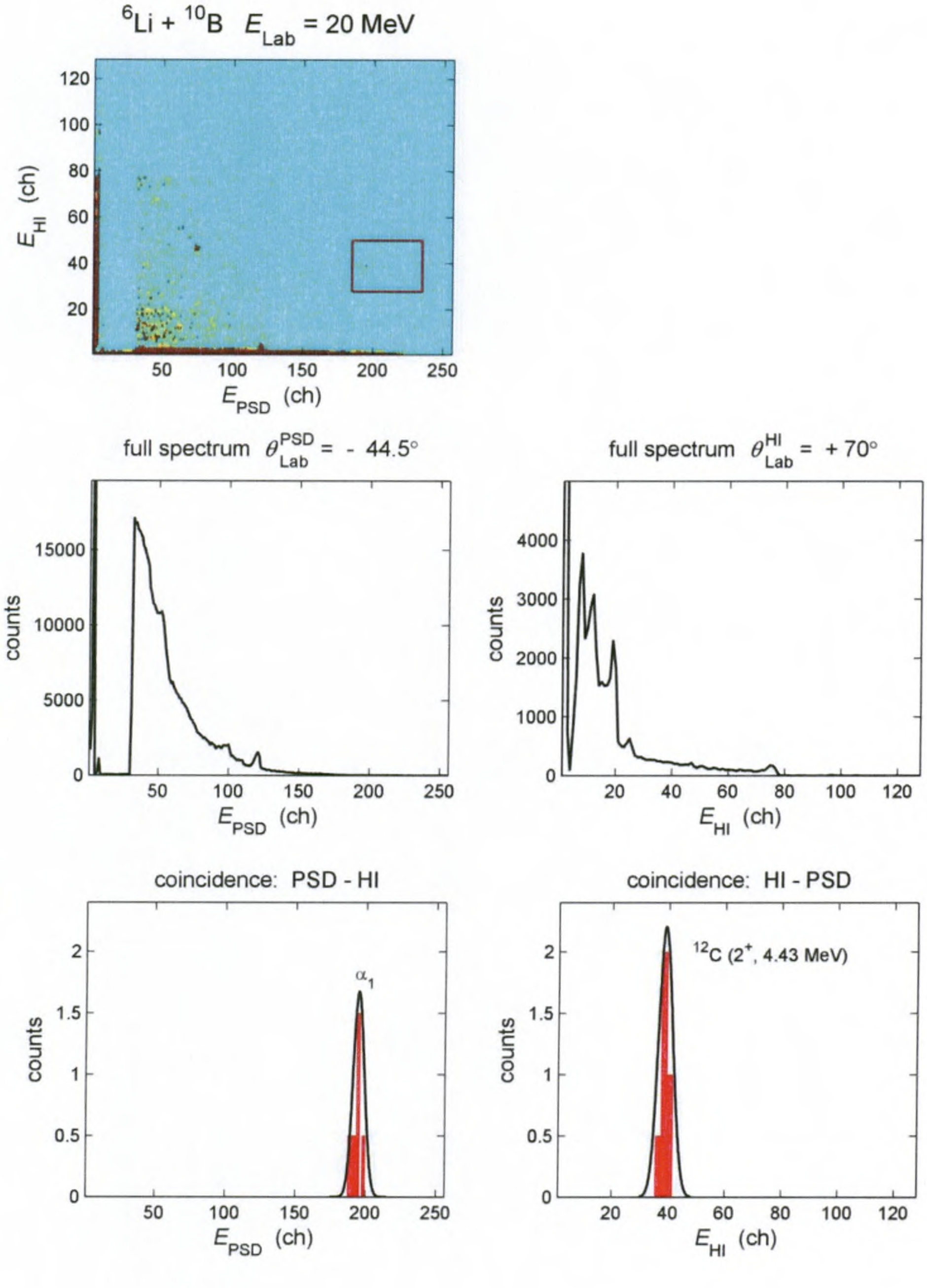

Figure 4.13: Preliminary angular distribution measurement for the ^{10}B (^{6}Li, α_n) ^{12}C* reaction at E_{Lab} = 20 MeV corresponding to $\theta_{\text{Lab}}^{\text{PSD}} = -44.5^{\circ}$ and $\theta_{\text{Lab}}^{\text{HI}} = +70^{\circ}$ with the projections of α_n and ^{12}C for the kinematic coincidence region indicated by the red rectangle in the upper left panel.

Table 4.3: Kinematic energies for the ^{10}B (^6Li, α_1) ^{12}C (2_1^+, 4.43 MeV) at E_{Lab}= 20 MeV

Angles θ_{HI}	E_{PSD} (α_1) (MeV)	E_{HI} $^{12}C(2_1^+$, 4.43 MeV) (MeV)
40°	21.738	17.532
50°	25.735	13.535
60°	29.563	9.707
70°	32.838	6.432

Table 4.4: Preliminary angular distribution results for ^{10}B (^6Li, α_1) ^{12}C (2_1^+, 4.43 MeV).

$^{10}B(^6Li,\alpha_n)^{12}C^*(J^\pi, E_x)$ E_{Lab} = 20 and 18.143 MeV							
E_{Lab} (^6Li) (MeV)	Angles $\theta_{c.m.}$	θ_{PSD}	θ_{HI}	^{12}C (2_1^+) (counts)	Runtime (hr)	Average beam current (enA)	$^{12}C(2_1^+)$ (counts/hr enA)
20	103.3°	−91.0°	+40.0°	5	1.00	12	0.42±0.21
20	89.9°	−74.2°	+50.0°	15	2.50	10	0.60±0.20
18.143	91.3°	−76.0°	+50.0°	24	8.00	6	0.50±0.14
20	73.2°	−59.3°	+60.0⁰	9	1.00	10	0.90±0.35
20	57.7°	−46.1°	+70.0⁰	5	0.50	12	0.83±0.41

4.4 Discussion

The correct functioning and linearity of the kinematic coincidence system comprising a silicon surface-barrier position sensitive detector and a singles silicon surface-barrier detector was demonstrated in Section 4.1. For this purpose elastic scattering of ^{12}C + ^{12}C at E_{Lab} = 22.5 MeV was employed. It was particularly useful to obtain a ^{12}C energy calibration for the singles silicon detector which would detect the ^{12}C product produced in the subsequent ^{10}B (^{6}Li, α_n) $^{12}C^*$ reaction measurement.

The investigation of the ^{10}B (^{6}Li, α_n) $^{12}C^*$ (J^π, E_x) reaction at an incident energy of E_{Lab} (^{6}Li) = 18.143 MeV was performed in order to determine the states in ^{12}C that were populated by the reaction. Cross sections were expected to be small and a long experimental run of approximately 8 hours was required to obtain distinct coincidence peaks in the data. Only the α_0 and α_1 channels were populated, corresponding to the production of the ^{12}C (0_1^+, g.s.) and ^{12}C (2_1^+, 4.43 MeV) states, respectively, with the α_1 channel being the most strongly populated (see Fig. 4.9). Here, it is suspected that the random coincidences result in the small yield above α_1 peak in the coincidence spectrum. As anticipated, states populated by the transfer reaction above the α_1 peak lead directly to 3α break-up and as such are not present to be detected by the coincidence measurement.

Further, a preliminary investigation into the yield of the α_0 and α_1 channels as a function of centre-of-mass angle showed that the α_1 channel is more strongly populated at the more forward centre-of-mass scattering angles.

CHAPTER 5

Conclusions

The initial set-up and calibration of the heavy-ion kinematic coincidence system provided the basis for investigating a nuclear transfer reaction. A relatively large acceptance angle for the silicon surface-barrier position sensitive detector allowed for the possible detection of a large excitation energy range in ^{12}C ($13 \leq E_x \leq 0$ MeV) provided by the reaction ^{10}B (^{6}Li, α_n) ^{12}C by detecting the corresponding α-particles produced. At an incident beam energy of E_{Lab} = 20 MeV above the Coulomb barrier for ^{6}Li + ^{10}B scattering, $E_{\text{Lab}}^{\text{CB}}$ = 6.216 MeV, and a relatively high Q-value = 23.713 MeV for the reaction, high energy α–particles are produced at energies well above those evaporation α–particles from compound nucleus reactions. This allowed for clear identification of the 0_1^+ ground state and the first and the first 2_1^+ state at 4.43 MeV in ^{12}C. The transfer reaction was found to be clearly selective, populating the 2_1^+ in ^{12}C by an order of magnitude more strongly than the 0_1^+ ground state.

As expected though, states in ^{12}C above the 2_1^+ state were not seen in the coincidence measurement since the 0_2^+ state at 7.65 MeV (Hoyle state) and the strong 3_1^- state at 9.64 MeV are above the 3α break-up threshold for excited ^{12}C. It was demonstrated that there is a measurable cross-section for the ^{10}B (^{6}Li, α_n) ^{12}C transfer reaction at incident energies not far above the Coulomb barrier and that the deuteron transfer is a very final-state spin selective. As such, the 0_2^+ Hoyle state and the 3_1^- at 9.64 MeV are also expected to be suppressed in favour of exciting 2^+ states. This leads to the conjecture that the 2^+ excited state of the Hoyle state, at excitation energy of 9.75 MeV in ^{12}C (beneath the strong 3_1^- state) could be measured clearly in future experimental work.

References

[AJZ59] F. Ajzenberg-Selove and T. Lauritsen, *Energy levels of light Nuclei,* Nuclear Physics II (1959) 1-340.

[AUE78] E. H. Auerbach, *A-THREE: A general optical model code especially suited to heavy-ion calculations*, Computer Physics Communications 15 (1978) 165-192.

[BUC06] L. R. Buchmann and C. A. Barnes, *Nuclear reactions in stellar helium burning and later hydrostatic burning stages*, Nuclear Physics **A777,** (2006) 254.

[CAT05] Wilton Catford, Relativistic kinematics programme in excel Catkin V2.02, http://www.ph.surrey.ac.uk/~phs1wc/kinematics, (2005).

[FEA92] R. W. Fearick, WIMPS2 *a multi-parameter data acquisition system* OS/2 *computer programme*, (1992).

[FRE09] M. Freer, H. Fujita, Z. Buthelezi, J. Carter, R. W. Fearick, S. V. Foertsch, R. Neveling, S. M. Perez, P. Papka, F. D. Smit, J. A. Swartz, and I. Usman, *2^+ excitation of ^{12}C Hoyle state*, Physical Review C80, 041303(R) (2009).

[FRE012] M. Freer, M. Itoh, T. Kawabata, H. Fujita, H. Akimune, Z. Buthelezi, J. Carter, R. W. Fearick, S. V. Fortsch, M. Fujiwara, U. Garg, N. Hashimoto, K. Kawase, S. Kishi, T. Murakami, K. Nakanishi, Y. Nakatsugawa, B. K. Nayak, R. Neveling, S. Okumura, S. M. Perez, P. Papka, H. Sakaguchi, Y. Sasamoto, F. D. Smit, J. A. Swartz, H. Takeda, S. Terashima, M. Uchida, I. Usman, Y. Yasuda, M. Yosoi, and J. Zenihiro, *Consistent analysis of the 2^+ excitation of the ^{12}C Hoyle state populated in proton and α-particle inelastic scattering*, Physical Review C86, 034320 (2012).

[FRE14] Martin Freer, *The structure of ^{12}C*, Indian Academy of science, Vol. 83, No 5 (2014).

[FYN04] H. O. U. Fynbo, C. Aa. Diget, Y. Prezado, J. Aysto., U. C. Bergmann, J . Cederkall, P. Dendooven, L. M. Raile, S. Franchoo, B. R. Fulton, W. Huang, J. Huikari, H. Jeppesen, A. Jokinen, B. Jonson, P. Jones, U. Koster, M. Hleister, T. Kilsson, G. Nyman, M. J. G. Borge, K. Riisager, S. Rinta-Antila, I. Storgaard Vogelius, O. Tengblad, M. Turrion, Y. Wang, L. Weissman, K. Wilhelmsen, and the ISOLDE Collaboration, *News on ^{12}C from β-decay studies*. Nuclear Physics A738, (2004) 59-65.

[GAB08] Gabor Gyulakis, *Proton induced reactions and the astrophysical process*, PhD thesis submitted to Institute of Nuclear Research of the Hungarian Academy of sciences (ATOMKI) (2008).

[HOD78] P. E. Hodgson, *Nuclear heavy-ion reactions,* Oxford University Press (1978).

[HOY54] F. Hoyle, The Astrophysical Journal, Supplement Series, vol.1 p.12, (1954).

[JAC70] Daphne F. Jackson, *Nuclear Reactions,* Muthuen & Co Ltd, (1970).

[JEL90] N. A. Jelly, *Fundamentals of nuclear physics,* Cambridge University Press (1990).

[JIN10] M. Jingo *Characteristics and use of a high resolution ΔE-E gas-ionisation detector for nuclear particle identification*, MSc Research Report, University of the Witwatersrand, (2010).

[KAR16] Karlsruhe Gamow window calculator, http://www.kadonis.org/process/gamow.php

[KHE15] Y. N. Kheswa, *iThemba LABS Target making laboratory*, Private communication (June 2015).

[KRA88] Kenneth S. Krane, *Introductory Nuclear Physics*, John Wiley & Sons, New York (1988) 378-440.

[MAR08] Martin Freer and K600 Group, *Progress report on the investigation of the possible excited states belonging to the triple alpha state in* ^{12}C, (2008).

[MAR68] J. B. Marion and F. C. Young, *Nuclear Reaction Analysis,* University of Maryland (1970).

[OST07] Ostlie, D. A & carroll, B. W. *An Introductory to Modern stellar Astrophysics*, Addison Wesley, San Francisco, (July 2007) ISBN 0-8053-0348-0.

[ORT68] **ORTEC** Instruction Manual Surface Barrier Detectors, (1968).

[ORT74] **ORTEC** Position Sensitive Detectors Analyser Manual, (1974).

[SAT80] G. R. Satchler, *Introduction to Nuclear Reactions,* Macmilan Press Ltd. (1980).

[WIL91] W. S. C. William, *Nuclear and particle physics,* University of Oxford (1991).

[ZAG16] V. I. Zagrebaev, A. S Denikin (denikin@jinr.ru), A. V. Karpov (karpov@jinr.ru), A. P. Alekseev, V. A. Rachkov, M. A. Naumenko, V. V. Samarin (samarin@jinr.ru), *Nucleon Transfer within Distorted Wave Born Approximation,* (2016).

[ZIM13] William R. Zimmerman, *Direct Observation of the second* 2^+ *state in* ^{12}C, PhD Thesis submitted to University of Connecticut (2013).